

# Astrocyte immunometabolic regulation of the tumour microenvironment drives glioblastoma pathogenicity

✉ Rita Perelroizen,<sup>1,†</sup> ✉ Bar Philosof,<sup>1,†</sup> ✉ Noga Budick-Harmelin,<sup>2</sup> ✉ Tom Chernobytsky,<sup>2</sup> Ariel Ron,<sup>1</sup> Rotem Katzir,<sup>3</sup> ✉ Dor Shimon,<sup>2</sup> ✉ Adi Tessler,<sup>2</sup> Orit Adir,<sup>2</sup> ✉ Anat Gaoni-Yogev,<sup>2</sup> Tom Meyer,<sup>1</sup> Avivit Krivitsky,<sup>2</sup> Nuphar Shidlovsky,<sup>2</sup> ✉ Asaf Madi,<sup>4</sup> ✉ Eytan Ruppin<sup>3</sup> and ✉ Lior Mayo<sup>1,2</sup>

<sup>†</sup>These authors contributed equally to this work.

Malignant brain tumours are the cause of a disproportionate level of morbidity and mortality among cancer patients, an unfortunate statistic that has remained constant for decades. Despite considerable advances in the molecular characterization of these tumours, targeting the cancer cells has yet to produce significant advances in treatment. An alternative strategy is to target cells in the glioblastoma microenvironment, such as tumour-associated astrocytes. Astrocytes control multiple processes in health and disease, ranging from maintaining the brain's metabolic homeostasis, to modulating neuroinflammation. However, their role in glioblastoma pathogenicity is not well understood. Here we report that depletion of reactive astrocytes regresses glioblastoma and prolongs mouse survival. Analysis of the tumour-associated astrocyte transcriptome revealed astrocytes initiate transcriptional programmes that shape the immune and metabolic compartments in the glioma microenvironment. Specifically, their expression of CCL2 and CSF1 governs the recruitment of tumour-associated macrophages and promotes a pro-tumourigenic macrophage phenotype. Concomitantly, we demonstrate that astrocyte-derived cholesterol is key to glioma cell survival, and that targeting astrocytic cholesterol efflux, via ABCA1, halts tumour progression. In summary, astrocytes control glioblastoma pathogenicity by reprogramming the immunological properties of the tumour microenvironment and supporting the non-oncogenic metabolic dependency of glioblastoma on cholesterol. These findings suggest that targeting astrocyte immunometabolic signalling may be useful in treating this uniformly lethal brain tumour.

- 1 Sagol School of Neuroscience, Tel Aviv University, Tel Aviv, Israel
- 2 Shmunis School of Biomedicine and Cancer Research, George S. Wise Faculty of Life Sciences, Tel Aviv University, Tel Aviv, Israel
- 3 Cancer Data Science Laboratory (CDSL), National Cancer Institute (NCI), National Institutes of Health (NIH), Bethesda, MD, USA
- 4 Sackler Faculty of Medicine, Tel Aviv University, Tel Aviv, Israel

Correspondence to: Lior Mayo Shmunis  
School of Biomedicine and Cancer Research  
George S. Wise Faculty of Life Sciences  
Tel Aviv University, Tel Aviv 69978, Israel  
E-mail: liormayo@tauex.tau.ac.il

**Keywords:** glioma; cholesterol; astrocytes

**Abbreviations:** ACM = astrocyte-conditioned medium; CM = condition media; DT-A = diphtheria toxin A; ECAR = extracellular acidification rate; FACS = fluorescence-activated cell sorting; FCS = foetal calf serum; GBM = glioblastoma multiforme; GCV = ganciclovir; GFP = green fluorescent protein; IDH = isocitrate dehydrogenase; iDTR = induced diphtheria toxin; iNOS = inducible nitric oxide synthase; LPDS = lipoprotein-deficient serum; OCR = oxygen consumption rate; OXPHOS = oxidative phosphorylation; TAA = tumour-associated astrocytes; TAM = tumour-associated macrophages; TCGA = The Cancer Genome Atlas; TME = tumour microenvironment

## Introduction

Cancers develop in complex tissue-dependent environments, on which they rely for sustained growth, response to therapy and regulate of the immune response to the tumours.<sup>1</sup> Unlike the tumour cells, non-neoplastic cells in the tumour microenvironment (TME) are genetically stable and thus represent an attractive therapeutic target, with a lower risk of resistance and tumour recurrence. Accumulating data suggest that modulation of the bioenergetic,<sup>2–4</sup> metabolic<sup>5,6</sup> or immunological<sup>7–11</sup> properties of the TME can regulate tumour progression in the CNS. However, the mechanisms that shape the immunometabolic landscape of the TME, and thus control brain cancer pathogenesis, are not well understood.

Glioblastoma multiforme (GBM) is the most common primary malignant brain tumour and carries an abysmal 5-year survival rate of just 5.6%, a statistic that, regrettably, has shown little change over decades.<sup>12,13</sup> Despite significant advances in our understanding of this disease, the translation to improved treatment has been quite disappointing. As a result, surgery, radiation and cytotoxic chemotherapy remain the mainstays of therapy, although immune checkpoint therapy has recently been suggested as a potentially efficacious approach.<sup>10,14</sup> Astrocytes are the most abundant cells in the CNS. They perform essential functions during development and homeostasis, such as participating in the maintenance of the blood–brain barrier, storing and distributing energetic substrates to neurons and supporting the development of neural cells and synaptogenesis.<sup>15,16</sup> Astrocytes can also control CNS inflammation and neurodegeneration through multiple mechanisms, including neurotoxicity, modulation of microglial activities, recruitment of inflammatory cells into the CNS and even via their metabolic cascade.<sup>17–23</sup> Tumour-associated astrocytes (TAAs) were recently suggested to participate in shaping the TME of primary and secondary brain tumours.<sup>24,25</sup> However, the role of reactive astrocytes in GBM pathogenicity is poorly understood.

Here we report that depletion of reactive TAAs regresses GBM progression in mice and prolongs animal survival. In addition, we found that astrocytes support the tumour by regulating the recruitment of tumour-associated macrophages (TAMs) to the TME via CCL2, and by promoting a pro-tumourigenic phenotype in the TAMs, partially via the release of CSF1. We also found that glioma cells depend on astrocyte-derived cholesterol for survival and, accordingly, targeting the cholesterol efflux from TAAs halts tumour growth. These findings explain the role of astrocytes in GBM pathogenesis and define the molecular circuits by which the astrocytes shape the immunometabolic landscape of the TME and control tumour progression, thereby identifying potential druggable candidates for therapeutic intervention.

## Materials and methods

### Animals

C57BL/6J, *Gfap*-TK [B6.Cg-Tg(*Gfap*-TK)7.1Mvs/J], *Gfap*-CRE [B6.Cg-Tg(*Gfap*-cre)77.6Mvs/2], from founder line 77.6, stock no 024098],

induced diphtheria toxin (iDTR) [Gt(ROSA)26Sor<sup>tm1(HBEGF)Awai</sup>] and RiboTag (B6N.129-Rpl22tm1.1Psam/J) mice were purchased from Jackson Laboratory (ME, USA). Female *Gfap*-TK<sup>+/-</sup> mice were crossed with male C57BL/6J to generate *Gfap*-TK<sup>+/-</sup> or wild-type (WT) mice. Female *Gfap*-Cre<sup>+/-</sup> were crossed with male RiboTag<sup>fl/fl</sup> or iDTR<sup>fl/fl</sup> to generate F1 littermates of *Gfap*Cre<sup>+/-</sup>-RiboTag<sup>fl/fl</sup> or *Gfap*-Cre<sup>+/-</sup>-iDTR<sup>fl/fl</sup> or *Gfap*Cre<sup>-/-</sup>-iDTR<sup>fl/fl</sup> mice. All animals were kept in a pathogen-free facility at the Tel Aviv University Faculty of Medicine and were housed five animals per cage under a standard light cycle (12 h:12 h light:dark) with *ad libitum* access to water and food. All experiments were carried out in accordance with guidelines prescribed by the Institutional Animal Care and Use Committee of Tel Aviv University.

### Cell lines

GL261-Luc2 cells (#9361, Caliper), CT-2A-Luc2 (#SCC195, Merck Ltd), U87EGFRvIII<sup>26</sup> (kindly provided by Dr Paul S. Mischel, Stanford University, CA, USA) and 293T AAVpro cells (#632273, Takara) were grown in Dulbecco's modified Eagle medium (DMEM) (Gibco #41965-039) with 10% foetal bovine serum (Gibco #12657-029) and 1% penicillin-streptomycin (Gibco #15140-122). The 293T medium was further supplemented with non-essential amino acids (BI, #01-340-1B) and 1% sodium pyruvate (BI, #03-042-1B). Cells were maintained free of mycoplasma contamination; routine mycoplasma analysis was performed using the EZ-PCR<sup>TM</sup> Mycoplasma Detection Kit (BI #2-700-20). In lipoprotein starvation experiments, normal foetal calf serum (FCS) was replaced with lipoprotein-deficient serum (LPDS, Sigma-Aldrich, #S5394).

### Primary glial cultures

Primary murine mixed glia (astrocytes and microglial cells) and astrocytes were prepared as we previously described.<sup>19</sup> Primary astrocytes cultures were found to be >99% GFAP-positive by immunofluorescent staining (Supplementary Fig. 5E). Microglial cultures were isolated by subjecting confluent mixed glial cultures to mild trypsinization (0.05% Trypsin in DMEM) according to previously published protocols.<sup>27</sup> This results in the detachment of an intact layer of cells containing virtually all the astrocytes, leaving undisturbed a population of firmly attached cells. Primary microglial cultures were identified as >99% IBA1<sup>+</sup> by immunofluorescent staining, and ~97.8% positive for the microglial marker CD11b (1:50; M1/70, BioLegend #101251) and negative for the astrocyte marker GLAST (1:11, ACSA-1, Miltenyi Biotec, #130-095-821) by fluorescence-activated cell sorting (FACS) analysis (Supplementary Fig. 5E and F). The following reagents were used for analysis: anti-IBA1 (1:500, Wako Chem, #019-19741), anti-GFAP (1:500, 4A11, 1B4, 2E1, BD Pharmingen #556330), anti-CD11b (1:50; M1/70, BioLegend #101251) and anti-GLAST (1:11, ACSA-1, Miltenyi Biotec, #130-095-821). For microglial proliferation analysis, pure microglial cultures were stained with CellTrace<sup>TM</sup> Violet Cell Proliferation Kit (Invitrogen, #C34517), according to the

manufacturer's instructions. Human astrocytes (ScienceCell, #1800) were grown according to the manufacturer's instructions. In some studies, cells were treated with 2 mM N-nitro-L-arginine methyl ester hydrochloride (L-NAME, Sigma, N5751), or anti-mouse CSF1R monoclonal antibody (mAb) (BioXcell, clone AFS98, #BE0213), anti-mouse TGF $\beta$  mAb (BioXcell, clone 1D11.16.8, #BE0057), anti-mouse IL10R mAb (BioXcell, clone 1B1.3A, #BP0050), anti-mouse IFN $\gamma$  mAb (BioLegend, clone XMG1.2, 505834), anti-mouse IL6R mAb (BioXcell, clone 15A7, #BE0047) or appropriate isotype control IgG (BioXcell, #BE0090, BE0090). All mAbs were used at a final concentration of 25  $\mu$ g/ml.

### Preparation of glioblastoma-conditioned medium

A total of  $2 \times 10^6$  GL261 cells were cultivated in a 10 cm culture plate for 48 h, media was removed and 8 ml of fresh medium, containing DMEM with 1% FCS and 1% penicillin-streptomycin was added. The supernatant was collected after 24 h, centrifuged at 500g for 10 min at 4°C, sterile filtered using a 22- $\mu$ m filter and stored at –80°C. For microglial stimulation, glioblastoma-conditioned medium (GBM-CM) was diluted 2:1 with DMEM.

### Preparation of astrocyte-conditioned medium

A total of  $5 \times 10^6$  primary astrocytes were cultivated in a 10 cm culture plate, and stimulated for 12 h with DMEM containing 1% FCS and 1% penicillin-streptomycin [to generate astrocyte-conditioned medium (ACM)] or GBM-CM (to generate T-ACM). Media was removed and 8 ml of fresh medium, containing DMEM with 0.5% BSA (Millipore, #810683) and 10 mM HEPES, was added. The supernatant was collected after 24 h, centrifuged at 500g for 10 min at 4°C, sterile filtered using a 22- $\mu$ m filter and stored at –80°C.

### Chemotaxis assay

Spleen monocytes (CD11b<sup>+</sup>/CD3<sup>–</sup>/CD45R<sup>–</sup>/CD117<sup>–</sup>/Ly-6G<sup>–</sup>/NK1.1<sup>–</sup>/SiglecF<sup>–</sup>/SSC<sup>low</sup>) were isolated from C57BL/6 mice using EasySep Mouse Monocyte Isolation Kit (Stemcell, #19861). Monocytes were stained with CellTrace CFSE Cell Proliferation (Thermo Fisher Scientific, #C34554) and a total of  $2 \times 10^3$  monocytes per well were plated in IncuCyte ClearView 96 well Cell Migration Plate (Sartorius, #4582), which was precoated with 50  $\mu$ g/ml Matrigel<sup>®</sup> (Corning, #FAL356237). ACM or T-ACM were added to the lower chamber and monocytes migration to the lower chamber was measured following 2 h incubation at 37°C with IncuCyte ZOOM (v.2020C). The chemotaxis index was defined as the percentage of monocytes that infiltrated the lower chamber. In some experiments, the T-ACM was supplemented with 30  $\mu$ g/ml of anti-mouse CCL2 neutralizing mAb (BioXcell, clone 2H5, #BE0185) or isotype control (BioXcell, #BE0091).

### Tumour model and treatments

For intracranial mouse glioma, mice were anaesthetized, positioned in a Stereotaxic Alignment System and injected with  $1.5 \times 10^4$  GL261 or CT-2A cells in 2  $\mu$ l of DMEM. Injections were made to the right frontal lobe, ~2.5 mm lateral and 0.1 mm caudal from bregma at a depth of 3 mm. *In vivo* bioluminescence imaging, following Xenolight D-luciferin potassium salt (150 mg/kg) i.p. administration, was determined using the IVIS Spectrum system (PerkinElmer). Ganciclovir (GCV, Cymevene, Roche #SAP-10051872; 25 mg/kg), diphtheria toxin (DT, Sigma-Aldrich, #D0564; 1100 ng/mice nasally) or vehicle control (PBS) were

administered daily following tumour establishment (Day 10), as previously described.<sup>19,28</sup> CD8<sup>+</sup> T-cell depletion was performed using an anti-CD8 monoclonal antibody (53.6-7, Bioxcell) or an isotype control monoclonal antibody (2A3, Bioxcell), as previously described.<sup>9</sup> GBM-bearing mice were intraperitoneally injected (0.1 mg/mouse) with an anti-CD8 or an isotype control mAbs, 1 day before and 7 days after, GCV administration. CD8 T-cell depletion was validated by FACS analysis using a Sony SH800 FACS instrument (Sony Biotechnology). Data analysis was performed using FlowJo v.10 (TreeStar, USA). The following reagents were used for analysis: anti-CD45 (1:100; 30-F11, BioLegend, #103106), anti-CD3 $\epsilon$  (1:50; 145-2C11, BioLegend #100335) and anti-CD8a (1:100; 53-6.7, BioLegend, #100765).

### Immunofluorescence

Animals were perfused with ice-cold PBS, followed by 4% paraformaldehyde in 0.1 M PBS. Tissues were cryoprotected in 0.1 M PBS plus 30% sucrose and cut with cryostat into 10- $\mu$ m thick sections. Sections were blocked in 5% goat serum and 5% donkey serum containing 0.3% Triton<sup>™</sup> X-100 (Sigma-Aldrich, #9002-93-1) and 0.3 M Glycine (Holland Moran, #BP381-1), and incubated overnight at 4°C with following antibodies: GFAP (chicken, 1:1000, Abcam, #ab4674), IBA1 (rabbit, 1:1000, Wako Chem, #019-19741), HA (rat, 1:300, Roche, #11-867-423-001), MBP (chicken, 1:50, Chemicon #AB9348), NeuN (mouse, 1:100, EMD Millipore, #MAB377) DRAQ7 (1:500 BioLegend, #424001), Cleaved Caspase 3 (rabbit, 1:500, Cell Signaling Technology, #9664S), ABCA1 (rabbit, 1:200, Novusbio, #NB400-105), Annexin A2 (rabbit, 1:500, proteintech, #11256-1-AP), Ki67 (Rat, 1:500, Thermo Fisher Scientific, #14-6698-82), PD-L1 (Rat, 1:500, BioXcell, #BE0101) or CD74 (Rabbit, Clone EPR25399-94, 1:500, Abcam, # ab289885). The next day sections were washed five times and incubated with an appropriate fluorophore-conjugated goat secondary antibodies (1:500) from Abcam (#ab150167 or ab150176) or Thermo Fisher scientific (#A11037, A11020 or A32733) for 1 h at room temperature. Sections were mounted in Prolong<sup>™</sup> Gold containing DAPI (Invitrogen, P36935). Images were acquired using a Leica SP8 confocal microscope and Leica LAS AF software and processed using Fiji and LAS X. All settings were kept the same during image acquisition of comparable images including magnification, laser intensity and optical configuration.

### Analysis of TAMs

GL261-implanted mice were killed 17 days after implantation and single-cell suspension was prepared as we previously described.<sup>19</sup> In brief, mice were anaesthetized and perfused with 10 ml of PBS and the brain was isolated, enzymatically dissociated using collagenase type III (Worthington Biochemical, #LS004182) and DispaseII (Roche, #04942078001), and mechanically dissociated using gentleMACS<sup>™</sup> Dissociator. Myelin was removed by resuspending the homogenate in 25% Percoll solution, underlaid by 75% Percoll and overlaid with 5 ml HBSS. Centrifugation at 1000g for 30 min with slow acceleration and without breaks created a gradient that separated the cell pellet on the bottom from the myelin, which was carefully aspirated. Cells were carefully collected from the 75–25% interphase. TAMs (CD11b<sup>+</sup>CD45<sup>+</sup>) or microglial cells (CD11b<sup>+</sup>CD45<sup>dim</sup>) were analysed or sorted into TRIzol LS reagent (Invitrogen, #10296028) for RNA purification using Sony SH800 FACS (Sony Biotechnology). Data analysis was performed using FlowJo v.10 (TreeStar, USA). The following reagents were used for analysis: anti-CD11b (1:50; M1/70, eBioscience, #12-0112-82,

BioLegend #101251), anti-CD45 (1:100; 30-F11, BioLegend, #103116) and anti-PD-L1 (1:50; 10F.9G2, BioLegend, #124314).

### Filipin III staining

Filipin III was used to evaluate cholesterol content in the cells using FACS and immunofluorescence staining. Filipin III (Cayman Chemical Company, #70440) staining was performed at 100 µg/ml for 25 min at room temperature, as previously described.<sup>29</sup> For FACS analysis cells were first fixed with 0.5% in paraformaldehyde (Electron Microscopy Sciences, #15710; dissolved in PBS), stained and then analysed by CytoFLEX LX flow cytometer (Beckman Coulter) equipped with a 355 nm (UV) laser.

### Metabolic flux assays

Real-time extracellular acidification rate (ECAR) and OCR measurements were made with an XF-96 Extracellular Flux Analyzer (Seahorse Bioscience).  $1 \times 10^5$  cells were plated into each well of Seahorse X96 cell culture microplates and preincubated at 37°C for 24 h in 5% CO<sub>2</sub> in either FCS or LPDS supplemented media. The sensor cartridge for the Xfe96 analyser was hydrated in a 37°C non-CO<sub>2</sub> incubator a day before the experiment. OCR and ECAR were measured under basal conditions and after the addition of the following compounds: 1.5 µM oligomycin, 2 µM FCCP [carbonyl cyanide-4-(trifluoromethoxy)phenylhydrazine], 0.5 µM rotenone and 0.5 µM antimycin, 10 mM glucose and 50 mM 2-deoxy-D-glucose (all obtained from Sigma) as indicated. Data were expressed as the rate of oxygen consumption in pmol/min or the rate of extracellular acidification in mpH/min, normalized to DNA labelling in individual wells determined by the Hoechst 33342 staining. Results were collected with Wave software v.2.4 (Agilent).

### Cell viability assay

GL261, CT-2A or astrocytes were seeded at a density of  $1.5 \times 10^5$  cells per well in a six-well plate. Cells were treated for 72 h FCS- or LPDS-supplemented media for 5 days. In some studies, cells were treated with lovastatin (Thermo Scientific, #PH1285R) at 2.5 or 5 µM (GL261, CT-2A, astrocytes), 24(S)-hydroxy-cholesterol (Cayman Chemical Company, #10009931) at 2.5, 5 or 10 µM (GL261 cells) or at 1.25, 2.5, 5 µM (CT-2A cells) for 72 h, or 250 ng/ml cholesterol (Sigma-Aldrich, #C4951). Cell death was analysed by FACS analysis based using Annexin-V assay according to the manufacturer's instructions (BioLegend, #640951, 640941). Microglial cell death was determined by LDH Assay (Sigma-Aldrich, #4744934001) according to the manufacturer's instructions.

### Astrocyte-specific lentivirus

pLenti-GFAP-EGFP-mir30-sh *Abca1* (Fig. 6F) harbouring shRNA sequences against *Abca1* was cloned into the pLenti-GFAP-EGFP-mir30-shB4galt6 vector backbone<sup>19</sup> and replaced by validated *Abca1*-targeting shRNA sequence (MISSION<sup>®</sup> TRC shRNA clone #TRCN0000271860, Sigma-Aldrich), as we previously described.<sup>19</sup> Non-targeting shRNA vector (pLenti-GFAP-EGFP-mir30-shNT) was previously described.<sup>19</sup> pLenti-GFAP-CRISPRv2GFP-sgRNA vectors (Supplementary Fig. 8B), were generated by cloning the relevant single-guide RNA (sgRNA) to pLentiCRISPRv2GFP (Addgene #82416) as previously described.<sup>30</sup> The EF-1 $\alpha$  promoter, which drives the expression of the polyprotein Cas9-P2A-GFP, was then replaced with the gfaABC1D promoter (GeneArt, Thermo Fisher Scientific) using XbaI and EcoRI restriction enzymes (#R3101 and #R0145, New

England Biolabs). CRISPR-Cas9 sgRNA sequences were designed using the Broad Institute's sgRNA GPP Web Portal (<https://portals.broadinstitute.org/gpp/public/analysis-tools/sgrna-design>). All sequences are detailed in Supplementary Table 1. Lentivirus particles were then generated by transfecting  $3.9 \times 10^6$  293T cells using 24.4 µg PEI MAX (Polysciences, #24765-1) with 6.1 µg pLenti-GFAP-EGFP-mir30-shRNA or pLenti-GFAP-CRISPRv2GFP-sgRNA vectors with the packing plasmids [4.6 µg psPAX2 (Addgene, #12260) and 1.5 µg pMD2.G (Addgene, #12259)]. Forty-eight hours after transfection supernatant was concentrated using Lenti-X Concentrator (Takara, #631232) and stored at -80°C until use. The viral titer was determined using the quantitative real-time polymerase chain reaction (qPCR) Lentivirus titration kit (ABM, #LV900) according to the manufacturer's instructions.

### Immunoblotting

Cells were lysed in RIPA buffer supplemented with protease inhibitors (Cell Signaling). A total of 35 µg of sample was separated by 7.5, 10 or 12% Tris-Glycine gels, transferred to nitrocellulose membranes (Millipore) and developed with antibodies against anti-ABCA1 (rabbit, 1:1000; Novus Biologicals, #NB400-105), anti-low-density lipoprotein receptor (LDLR) (rabbit, 1:500, ProteinTech, #10785-1-AP), anti-ACTIN (mouse, 1:1000-30 000; MP Biomedicals, #08691001), anti- $\alpha$ -ACTININ (mouse, 1:1000; Cell Signaling Technology, #69758S) and anti-VINCULIN (rabbit, 1:1000, Proteintech, #26520-1-AP). Blots were developed using a Clarity Western ECL kit (Bio-Rad, #1705061) on Amersham Imager 600 (GE Healthcare). Expression levels were normalized to ACTIN,  $\alpha$ -ACTININ or VINCULIN. Quantification was done using Image Studio Lite software v.5.2 (LI-COR Biosciences).

### Metabolic pathway analysis

iMAT<sup>31</sup> was used to incorporate gene expression levels into the metabolic model to predict a set of high and low activity reactions. Network integration was determined by mapping the genes to the reactions according to the metabolic model, and by solving constraint-based modelling optimization to find a steady-state metabolic flux distribution.<sup>32</sup> By using the constraint-based modelling approach, we assign permissible flux ranges to all the reactions in the network, in a way that satisfies the stoichiometric and thermodynamic constraints embedded in the model and maximizes the number of reactions whose activity is consistent with their expression state. The pathway enrichment analysis was carried out by a hypergeometric test where the background is the number of reactions found in the human model, and the overlap of each metabolic pathway with the set of active (top 20%) and inactive reactions (low 20%) is then examined via hypergeometric test.

### nCounter gene expression

Total RNA (100 ng) was analysed using the nCounter Mouse Immunology V1 Panel according to the manufacturer's instructions (NanoString Technologies). Data were analysed using nSolver Analysis software. Functional enrichment analysis was performed using the Expander<sup>33</sup> and g:Profiler<sup>34</sup> platforms.

### RiboTag

Sham or tumour-bearing mice were sacrificed and were subjected to perfusion through the left ventricle with ice-cold PBS, followed

by perfusion with 10 ml ice-cold 1% PFA (Electron Microscopy Sciences, #15710; dissolved PBS). Brains were harvested, and the right hemisphere was homogenized as previously described.<sup>35</sup> Briefly, samples were homogenized using 7 ml Dounce homogenizer in 10% w/v supplemented homogenization buffer. Homogenate was transferred to an Eppendorf tube and centrifuged for 15 min at 15 000g at 4°C. The supernatant was transferred to a new tube and 5 µl of mouse monoclonal anti-HA antibody was added (BioLegend, #901515). Samples were placed on a rotator for 6 h at 4°C. Pierce beads (200 µl) (Pierce, #88803) or 70 µl of Dynabeads (Invitrogen, #10004D) were washed with 800 µl homogenization buffer and coupled with the tissue-antibody homogenate for an overnight rotation at 4°C. The following day, samples were placed on a magnet and the supernatant was removed before washing the pellets three times for 10 min in a high salt buffer. RLT lysis buffer (350 µl) was added to the beads and RNA was extracted using the RNeasy Mini kit (Qiagen, #74104) per the manufacturer's instructions and quantified with a Qubit RNA HS Assay Kit (Thermo Fisher, #Q32852). RNA was kept at –80°C until use.

### RNA-sequencing and processing

RNA extracted from immunoprecipitated polyribosomes was used to prepare libraries by NEBNext<sup>®</sup> rRNA depletion kit (#E6310), NEBNext<sup>®</sup> Ultra<sup>™</sup> II RNA Library Prep Kit for Illumina (#E7770G) and NEBNext<sup>®</sup> Multiplex Oligos for Illumina<sup>®</sup> (#E7335G) kit, according to the manufacturers' instructions. Libraries were normalized, pooled and sequenced on the Illumina NextSeq 500 with the NextSeq 500/550 Mid Output Kit v.2.5 (150 Cycles) (#20024904), according to the manufacturers' instructions. RNA-sequencing (RNA-seq) reads were aligned using Kallisto<sup>36</sup> to mouse genome v.mm10, and expression levels were calculated using RSEM.<sup>37</sup> The data were normalized using TMM normalization and differentially expressed genes were defined using the differential expression pipeline on the raw counts with a single call to the function Bioconductor package DESeq2 v.1.24.0 in R<sup>38</sup> (FDR-adjusted *P*-value <0.05). Heat map figures were generated using the pheatmap package<sup>39</sup> and clustered using Euclidian distance. Functional enrichment analysis was performed using the Expander<sup>33</sup> and g:Profiler<sup>34</sup> platforms.

### Human gene expression and survival analysis data

Bulk gene expression of matched GBM patients and normal brain tissue was analysed using the GEPIA portal<sup>40</sup> based on The Cancer Genome Atlas (TCGA) and Genotype-Tissue Expression (GTEx) datasets. *P* < 0.01 was considered statistically significant. Survival analysis was performed using the Chinese Glioma Genome Atlas (CGGA),<sup>41</sup> *P* < 0.05 was considered statistically significant. Single-cell analysis was performed on data of GBM patients [isocitrate dehydrogenase 1 (IDH1)-negative, grade IV] reported by Darmanis et al.<sup>42</sup> using Bbrowser<sup>43</sup> (v.2.10.40; BioTuring Inc.). Cell-lineage clusters were defined on the basis of the expression of known markers<sup>44,45</sup> (TAMs, PTPRC, C1QC and TMEM119; OPCs, PDGFRA, GPR17, OLIGO1 and AC058822.1; TAAs, SLC7A10, GJA1 and AQP4; Oligodendrocytes, MOBP and MOG; endothelial cells, CD34 and PECAM1).

### Statistical analysis

Samples were randomly allocated into experimental groups at the start of each individual experiment. Genetically identical mice were randomly allocated to experimental groups at the start of

the experiments. For *in vitro* experiments, biological samples were randomly allocated into experimental groups at the beginning of the experiment. Statistical analyses were performed with Prism v.9.3 software (GraphPad), and the statistical tests used are indicated in the individual figure legends. *P* < 0.05 was considered statistically significant. All error bars represent SEM. Box-and-whisker plots show median, interquartile interval, minimum and maximum values.

### Data availability

RNA-seq data that support the findings of this study have been deposited in the Gene Expression Omnibus GSE193526. All other data supporting the findings of this study are available from the corresponding authors on request.

## Results

### Tumour-associated astrocytes promote glioblastoma pathogenicity

Reactive astrocytes, characterized by elevated expression of glial fibrillary acidic protein (GFAP), have a considerable impact on the course of traumatic, ischaemic, inflammatory and degenerative diseases of the CNS.<sup>17,18</sup> Astrocytes are one of the most abundant non-cancerous cell types in glioblastoma,<sup>42</sup> and reactive astrocytes are present around the tumour margins (Fig. 1A). Accumulating *ex vivo* data concerning the cross-talk between astrocytes and glioma cells,<sup>24</sup> and specific inhibition of astrocytic signalling in medulloblastoma and brain metastasis tumour models,<sup>25,46,47</sup> suggest that astrocytes might play a role in glioblastoma progression. However, the role reactive astrocytes play in glioblastoma pathogenicity *in vivo* is not well understood.

To study the role of TAAs in glioblastoma, we analysed the course of tumour progression in mice expressing the herpes simplex virus thymidine kinase (HSVtk) under the *Gfap* promoter (*Gfap*-TK), in which GCV administration can deplete reactive and proliferating astrocytes.<sup>19,48,49</sup> For this purpose, we intracranially injected GFP\*GL261-Luc (GL261) glioma cells, into syngeneic C57Bl/6 wild-type or *Gfap*-TK littermates. Ten days after tumour implantation, once the tumours were established, the mice were treated with GCV for 7 days, before an examination of the presence of GFAP<sup>high</sup> reactive astrocytes at the tumour margins (Fig. 1B). In line with previous reports of the specificity and efficiency of the *Gfap*-TK model,<sup>19,48,49</sup> we found that GCV administration to GBM-bearing mice results in specific ablation of reactive astrocytes around the tumour in the *Gfap*-TK mice but not in wild-type mice (Fig. 1C). To test the functional contribution of reactive astrocytes to GBM progression, we repeated the same experimental paradigm, as in Fig. 1B, and evaluated the tumour growth by bioluminescence imaging and histology (Fig. 1D and E). While neither GCV treatment of wild-type mice nor genetic insertion of the HSVtk into *Gfap*-TK mice, affected GBM progression (Supplementary Fig. 1A and B), GCV treatment of GL261-bearing *Gfap*-TK mice did result in dramatic tumour regression (Fig. 1D and E). Of note, clinical trials aimed at over-expressing HSVtk in high-grade gliomas have shown minimal to no improvement in tumour burden and survival.<sup>50</sup> Collectively, these data suggest that depletion of TAAs halts glioma growth. To further validate these findings, we used an alternative astrocyte-depleting transgenic mice model, in which the DT receptor is expressed under the control of the murine *Gfap* promoter (*Gfap*CRE: iDTR, Supplementary Fig. 1C). Astrocytes are ablated in the

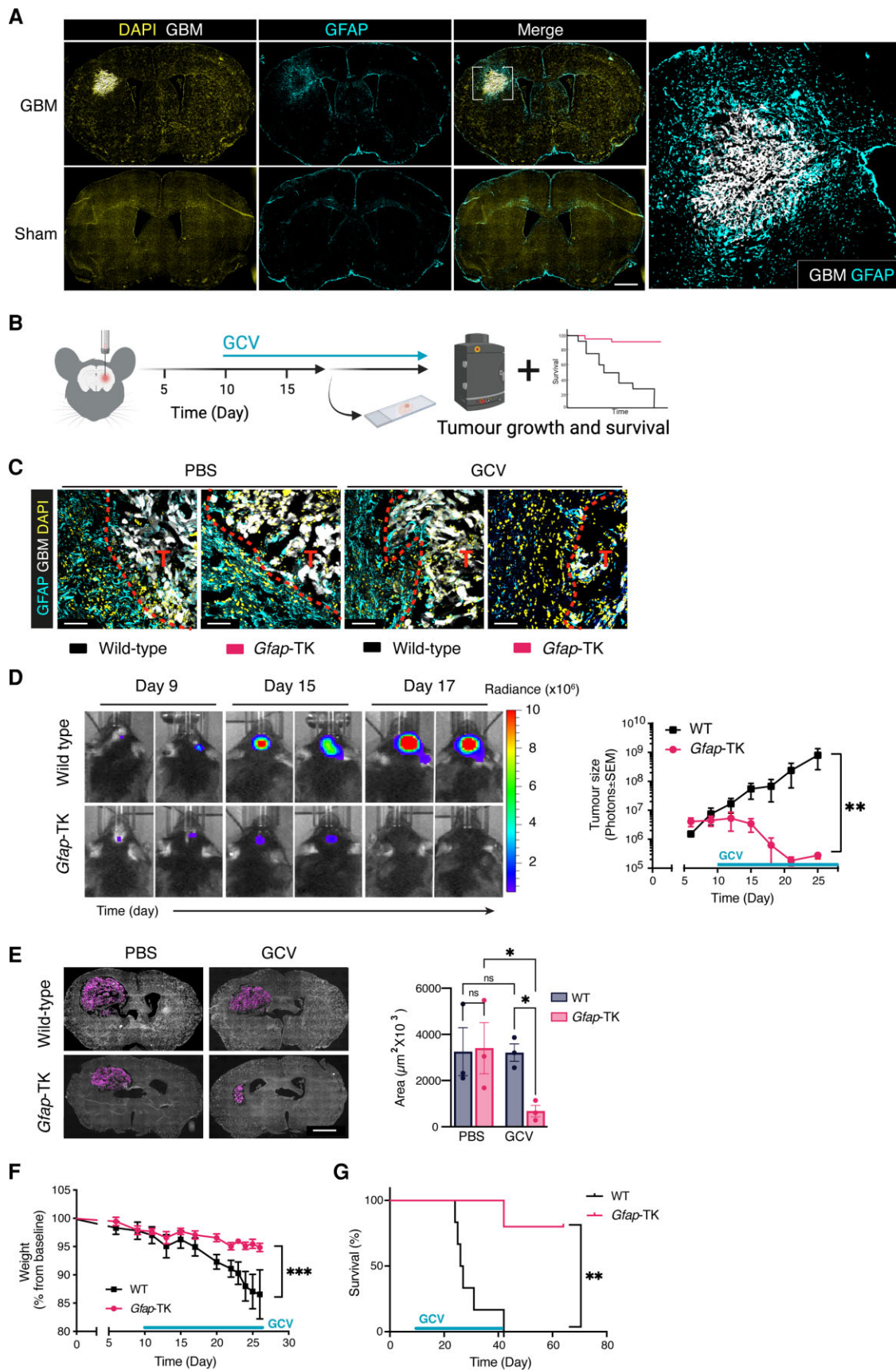


**Figure 1** TAA depletion regress GBM progression. (A) Representative immunofluorescence images of reactive TAAs stained for GFAP (cyan) crowning a glioblastoma (GBM) tumour (GFP<sup>+</sup>-GL261, white), and nuclei (DAPI, yellow). The right image is an expansion of the area marked by the white box. ( $n=3$  biologically independent experiments, three mice per group). Scale bar = 1000  $\mu\text{m}$ . (B–G) Wild-type (WT), or *Gfap*-TK

(Continued)

*Gfap* CRE:iDTR mice by administration of diphtheria toxinA (DT-A). We, therefore, crossed heterozygote *Gfap*CRE with homozygotes mice harbouring a Cre-inducible expression of DTR (iDTR). *Gfap*CRE:iDTR and iDTR littermates were intracranially implanted with GL261 gliomas, and were treated with DT-A once the tumours were established. The results indicate a significant regression in tumour size in the GL261-bearing *Gfap*CRE:iDTR mice, compared to their iDTR tumour-bearing littermates (Supplementary Fig. 1D), which is in agreement with the data obtained from the *Gfap*-TK astrocyte-depleting model (Fig. 1D).

Next, we examined the effect of astrocyte depletion on the disease pathophysiology. To this end, we intracranially implanted GL261 cells into wild-type or *Gfap*-TK littermates. The mice were treated with GCV (as in Fig. 1D) and the weight and survival were monitored. In accordance with the observed tumour regression, we found that astrocyte ablation significantly attenuates the weight loss in GL261-bearing *Gfap*-TK mice compared to their tumour-bearing wild-type littermates and dramatically improves their survival (Fig. 1F and G, respectively). In contrast, GCV administration to GL261-bearing wild-type mice, or expression of the HSVtk transgene without GCV treatment, had no effect on survival (Supplementary Fig. 1E and F). Interestingly, the high survival rate of the GL261-implanted *Gfap*-TK mice persisted even after GCV administration was terminated following the death of all the mice in the wild-type group (Fig. 1G). It should be noted that prolonged treatment (3–4 weeks) of the *Gfap*CRE:iDTR mice with DT-A led to lethal bowel inflammation, presumably due to ablation of GFAP<sup>+</sup> enteric glia in the distal small intestine. This was unrelated to tumour burden (data not shown), but as a result the *Gfap*CRE:iDTR model was only used to monitor tumour growth for a short regimen of DT-A treatment (7 days), well before the appearance of any DT-dependent clinical phenotype, and was not used in the survival studies. Importantly, our observations that astrocytes support tumour pathogenicity were validated by the finding of similar results in an alternative syngeneic GBM model (CT-2A glioma cells) (Supplementary Fig. 1G–I). Thus, these data suggest that reactive TAAs play a pivotal role in supporting glioma progression and tumour pathogenicity.

### Tumour-associated astrocytes acquire a pro-tumourigenic phenotype

To investigate the mechanisms by which reactive astrocytes support GBM pathogenicity, we first analysed their transcriptional programme using the RiboTag strategy, in which the expression of a haemagglutinin (HA)-tagged ribosome subunit, under the control of a CRE recombinase, allows for the analysis of cell-specific ribosome-associated mRNA. Mice carrying the floxed *Rpl22*-HA allele<sup>35</sup> (RiboTag mice) were crossed with *Gfap*CRE mice to generate *Gfap*CRE:*Rpl22*HA mice. To implement the RiboTag method for the study of TAAs, *Gfap*CRE:*Rpl22*HA mice were intracranially implanted with GL261 glioma cells (GBM) or injected with PBS

(sham). Seventeen days later, RNA was retrieved from mouse brain extract (input) by anti-HA immunoprecipitation (IP-HA, Fig. 2A). First, we examined the co-localization of the HA tag specifically with astrocytes in the *Gfap*CRE:*Rpl22*HA mice and the cell-type specificity of the obtained transcriptomes. Analysis of astrocyte-enriched RNAs (immunoprecipitated by an anti-HA antibody) confirmed enrichment of astrocyte-specific gene expression, and concomitant depletion of neuronal, oligodendroglial and macrophage-specific gene expression (Fig. 2B). This was further validated by immunostaining (Fig. 2C). As the next step, we examined the transcriptional phenotype of the reactive astrocytes in the GBM microenvironment. Principal component analysis demonstrated distinct differences between the TAAs (GBM) and the astrocytes isolated from the sham control group (Supplementary Fig. 2A). Indeed, we found that 3884 genes were differentially expressed (FDR-adjusted  $P$ -value  $< 0.01$ , fold change  $> 2$ ) between the two groups of astrocytes (Fig. 2D). These included an increased expression of immune-associated genes (*Chi3l1*, *Cd74*),<sup>24</sup> complement components (*C1s*, *C3*),<sup>24,51</sup> chemokines (*Ccl2*)<sup>52</sup> and proliferation (*Mki67*, *Anxa2*),<sup>24</sup> transcription factors associated with glial support of brain tumours (*Stat1*, *Stat3*, *Ahr*),<sup>9,53</sup> as well as genes associated with astrocyte cross-talk with microglial cells (*Csf1*, *Cd44*)<sup>7,8,54</sup> or immunosuppression (e.g. *Cd274*, *Gpnb*)<sup>24,55,56</sup> (Fig. 2E and Supplementary Fig. 2B and C). In line with our findings, analysis of single-cell RNA-sequencing data (scRNAseq) released by Darmanis et al.<sup>42</sup> of the TME of GBM patients (IDH1-negative, grade IV) identified a similar expression pattern in TAAs (Supplementary Figs 3A and B, and 4D). Functional analysis<sup>34</sup> of the differentially expressed genes, identified enrichments in three main categories, namely perturbation of metabolic process, immune regulation, and cell proliferation (Fig. 2F and Supplementary Table 2). Notably, the astrocyte immunosuppressive activity in the TME is not dependent on the CD8<sup>+</sup> T-cell response, as the latter depletion did not modulate astrocyte-driven GBM pathogenicity (Supplementary Fig. 2D and E). Thus, these data identify a distinct phenotype of TAAs in the glioblastoma microenvironment, whose transcriptomic characteristics resemble those of astrocytes from GBM patients. These results suggest that astrocytes might support glioma pathogenicity by directly promoting immunosuppression, regulating the neighbouring immune cells and contributing to the metabolic landscape of the TME.

### Astrocytes modulate the recruitment of GBM-infiltrating macrophages

The population of TAMs is made up of brain-resident microglia and monocyte-derived macrophages from the periphery.<sup>42,57,58</sup> Together, they account for 30–50% of the tumour mass, and their number is positively correlated with the tumour malignancy grade and inversely correlated with overall survival in patients with recurrent glioblastoma.<sup>57</sup> Astrocytes regulate leukocyte infiltration to the CNS through several mechanisms that range from the regulation of blood–brain barrier permeability to the secretion of chemokines.<sup>17,18</sup>

#### Figure 1 Continued

GBM-bearing mice were treated daily with GCV (25 mg/kg) from Day 10 until the experimental end point as illustrated in B. (C) representative immunofluorescence images of reactive-astrocyte depletion at the tumour margins (GFP<sup>+</sup>-GL261, white), as detected by GFAP (cyan) and nuclei staining (DAPI, yellow). Scale bars = 500  $\mu$ m. Data are representative of three independent experiments with  $n = 4$  mice/group. (D and E) Tumour size in GCV-treated wild-type or *Gfap*-TK GBM-bearing littermates. (D) Representative images of GL261-derived bioluminescence from each group are shown on the left and quantification of tumour size on the right. Data are representative of five independent experiments with  $n = 6$  mice/group. (E) Representative images from each group, 17 days after GL261 cell implantation, are shown on the left with quantification of tumour size on the right, tumour (GL261 cells in purple) and nuclei (DAPI; white). Scale bar = 1000  $\mu$ m. Data are representative of three independent experiments with  $n = 5$  mice/group. (F) Bodyweight assessment of mice from D. (G) Kaplan–Meier curves assessing overall survival. Data are representative of three independent experiments with  $n = 8$  mice/group. Data in D–F are shown as mean  $\pm$  SEM.  $P$ -values were determined by two-way ANOVA (D–F) or log rank (Mantel–Cox) test (G). \* $P < 0.05$ , \*\* $P < 0.01$ , \*\*\* $P < 0.001$ , n.s. = not significant.

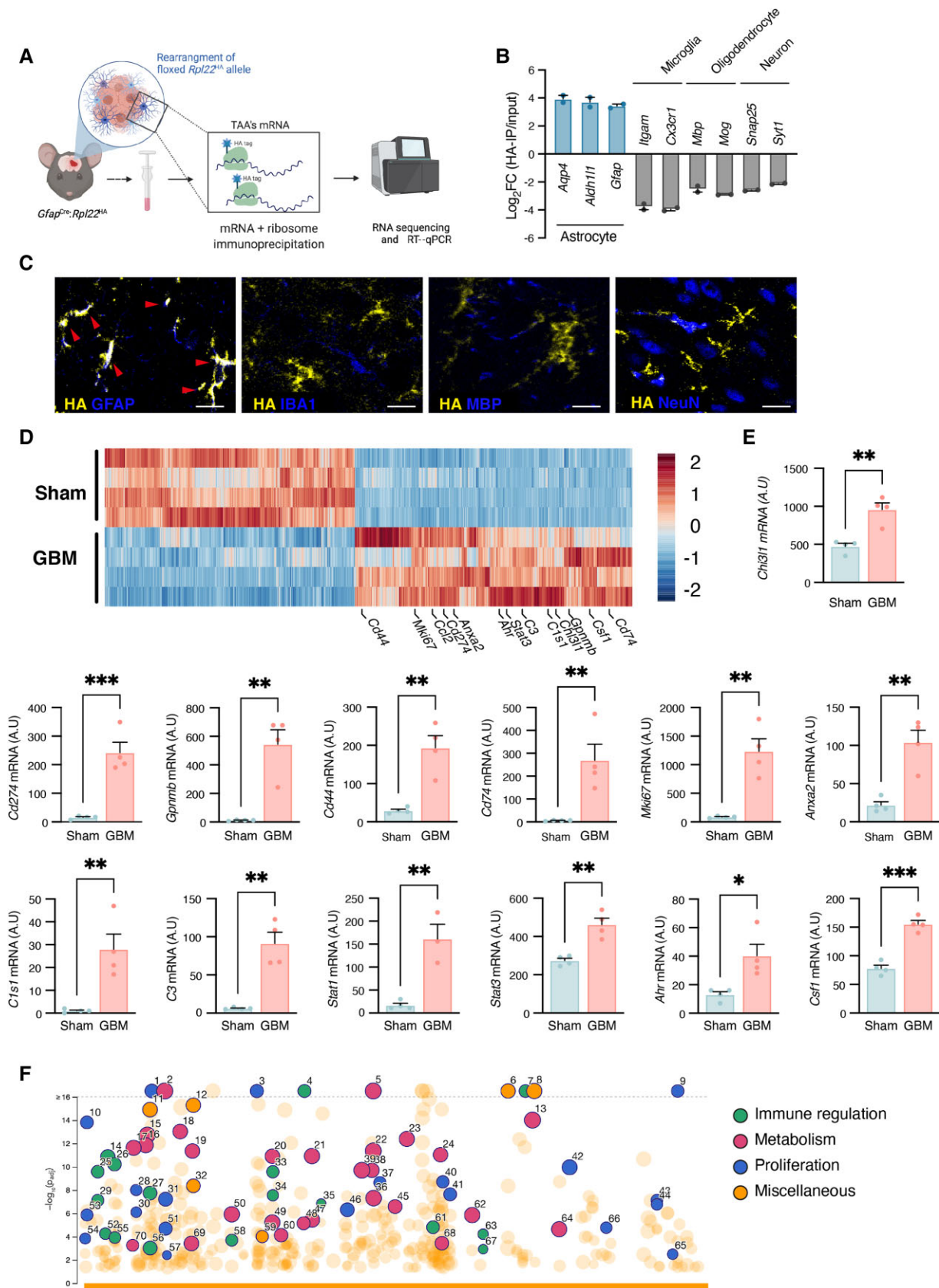


Figure 2 RiboTag analysis of TAAs reveals activation of immunoregulatory pathways and perturbation of metabolic circuits. (A) Illustration of the RiboTag workflow. (B) Enrichment of astrocyte-specific gene expression and de-enrichment of neuronal, oligodendroglial and TAMs gene expression, shown as the log fold change calculated between astrocyte RNAs immunoprecipitated by anti-HA antibody versus brain

(Continued)



Indeed, we found that TAAs significantly upregulate their chemoattractant profile, compared to astrocytes isolated from the sham control (Fig. 3A), of which CCL2 and CXCL16, chemokines associated with TAMs tumour-promoting activity,<sup>52,59</sup> were significantly expressed in astrocytes from GBM patients<sup>42</sup> (Fig. 3B). There are many factors that may mediate TAM chemoattraction to the GBM,<sup>57</sup> but the main pathway for the recruitment of peripheral macrophages to the TAM compartment is considered to be via CCR2 signalling, which is triggered by CCL2 and CCL7. Accordingly, our analysis of the GBM Genome Atlas data revealed high levels of expression of CCR2, CCL2 and CCL7, which were associated with decreased survival in glioblastoma patients (Supplementary Fig. 4A–C). Under neuroinflammatory conditions, astrocytes regulate leukocyte infiltration to the CNS through several mechanisms, including the secretion of CCL2.<sup>19,23,60</sup> However, the contribution of TAAs to the recruitment of TAMs during GBM progression is not well understood. To address this question, we first screened scRNAseq data from GBM patients<sup>42</sup> for astrocytic expression of CCL2 and CCL7. The results indicated that while astrocytes express high levels of CCL2, CCL7 was barely detectable (Supplementary Fig. 4D). Similarly, the levels of *Ccl2* were elevated in astrocytes isolated from GL261-bearing mice using the RiboTag system (Fig. 3C) and primary astrocytes treated with tumour-conditioned media generated using murine GL261 glioma (GBM-CM) (Fig. 3D). Interestingly, *Ccl7* expression was not detected in Ribotag-isolated astrocytes, or GBM-CM treated primary astrocytes. Accordingly, we found that ACM, harvested from GBM-treated astrocytes (T-ACM), was significantly more efficient in inducing monocyte migration than control ACM (Fig. 3E). Importantly, the use of anti-CCL2 neutralizing antibodies to block CCL2 signalling, inhibited this increase in monocyte migration, implicating CCL2 as the main chemoattractant in GBM-induced astrocyte recruitment of the monocytes (Fig. 3E). To investigate whether these observations indicate that TAAs regulate TAM recruitment to the TME, we monitored the recruitment of TAMs into the TME of GL261-bearing wild-type and *Gfap*-TK mice treated with GCV (as in Fig. 1B). We found that depletion of reactive astrocytes with GCV significantly reduces the accumulation of IBA-1<sup>+</sup> TAMs in the TME (Fig. 3F). Similar results were obtained by FACS analysis of the frequency of TAMs (CD11b<sup>+</sup>CD45<sup>+</sup>) cells in the TME (Fig. 3C), suggesting that reactive astrocytes directly control the recruitment of TAMs to the GBM TME and that this process is predominantly mediated by CCL2.

### Tumour-associated astrocytes direct TAMs towards an immunosuppressive phenotype

TAMs support glioblastoma pathogenicity, by promoting tumour growth, immunosuppression and resistance to therapy.<sup>9,57,61–65</sup> They acquire this distinct pro-tumour phenotype as a result of direct interactions with the tumour and the TME,<sup>57,66,67</sup> although the mechanisms concerned are not entirely understood. We have previously demonstrated that astrocytes regulate the immunological profile of resident microglial cells and CNS-infiltrating monocytes

during neuroinflammation<sup>19,23</sup> and Henrik Heiland *et al.*<sup>24</sup> reported a similar cross-talk between astrocyte and microglial cells in *in vitro* models of glioma. Thus, to investigate whether reactive astrocytes also control TAMs activity in the context of tumour pathology, we analysed the transcriptome from TAMs harvested from GL261-bearing wild-type and *Gfap*-TK mice that were treated with GCV (as in Fig. 1D) to deplete their reactive astrocytes (Fig. 4A–C and Supplementary Fig. 5A). We found that astrocyte depletion was accompanied by significant differences in the mRNA expression profile of TAMs. These changes were identified as factors associated with the functional enrichment of immune regulation pathways, TAM metabolome and regulation of cell death (Fig. 4A and Supplementary Fig. 5A). Notably, astrocyte depletion reduced the expression of a number of the hallmark genes associated with the tumour-promoting TAM phenotype,<sup>57,61–65</sup> including *Arg1*, *Mmp14*, *Stat3*, *Irf7*, *Gpnmb*, *Vegfa* and aryl hydrocarbon receptor (*Ahr*), which was recently shown to regulate TAMs activity in GBM<sup>9</sup> (Fig. 4B). Promoting immunosuppression is one of the mechanisms by which TAMs are known to contribute to GBM progression and resistance to emerging immunotherapies.<sup>57,68</sup> Programmed death-ligand 1 (PD-L1), encoded by *CD274*, is among the prominent members of the checkpoint inhibitor family and has shown promising therapeutic potential in a variety of different neuropathologies, including GBM.<sup>10,14,69</sup> Analysis of the scRNAseq data<sup>42</sup> derived from the TME of GBM patients reveals that the high expression of *CD274* seen by TCGA analysis in GBM patients can be attributed predominantly to TAMs and astrocytes. Importantly, a reduction in the expression of *CD274* is associated with improved survival (Supplementary Fig. 5B–D). We found that depletion of reactive astrocytes significantly attenuated *Cd274* induction and PD-L1 expression by TAMs (Fig. 4C and D), suggesting that TAAs program the TAMs to support GBM pathogenicity and induce an immunosuppressive environment. To test this hypothesis, we studied the effects of the presence or absence of astrocytes on the microglial expression of PD-L1 in response to GBM-CM stimulation (Fig. 4E). In line with our *in vivo* analysis (Fig. 4D), the expression of PD-L1 was inhibited in the absence of astrocytes (Fig. 4F). These data therefore support the notion that astrocytes can directly re-programme the microglial cells to promote the immunosuppressive profile of the TME.

Most microglial cells in non-malignant or regressing tumours have a pro-inflammatory activity that may promote tumour lysis. Accordingly, pro-inflammatory microglial cells, which express the inducible nitric oxide synthase (iNOS), have been shown to induce glioma cell death.<sup>57,70,71</sup> Our transcriptomic analysis suggests that astrocyte depletion regulates the TAMs cytotoxic potential and can modulate nitric oxide (NO) metabolism in the TME (Figs 2F and 4A and Supplementary Table 2). As the first step to confirm this possibility, we examined the ability of astrocytes to regulate the microglial-mediated glioma cytotoxicity (Fig. 4G and H). For this purpose, microglial cells were pre-activated with GBM-CM in the presence or absence of astrocytes for 24 h, to allow

#### Figure 2 Continued

total cell RNAs from the original homogenate (including astrocytes). (C) Representative immunofluorescence images of *Gfap*CRE:Rpl22HA mice demonstrating co-localization of ribosome-associated HA Tag (yellow) with specific cell-lineage markers of astrocytes, TAMs, oligodendrocytes or neurons cell-lineage specific markers (GFAP, IBA1, MBP or NeuN, respectively; blue). Co-localization (white) is identified by red arrowheads. Scale bars = 20  $\mu$ m. (D) Heat map of differentially expressed genes (at least 2-fold,  $P_{adj} < 0.01$ ) of astrocytes derived from sham-injected or GBM-bearing brain hemisphere specimens. (E) RiboTag-isolated mRNA expression in astrocytes from GL261-bearing (GBM) or PBS-injected (Sham) *Gfap*<sup>Cre</sup>:Rpl22<sup>HA</sup> mice; 17 days after intracranial injection. Data are representative of three independent experiments with  $n = 4$  biologically independent samples, pool of two mice per sample. (F) Manhattan plot of gene ontology (GO) of upregulated in TAAs. Similar pathways are colour-coded: Immune regulation (green), metabolism (pink), proliferation (blue), miscellaneous (orange). Highlighted GO are numbered and detailed in Supplementary Table 2. Data in B and E are shown as mean  $\pm$  SEM. P-values were determined by one-way ANOVA (B) or two-sided Student's t-tests (E). \* $P < 0.05$ , \*\* $P < 0.01$ , \*\*\* $P < 0.001$ .

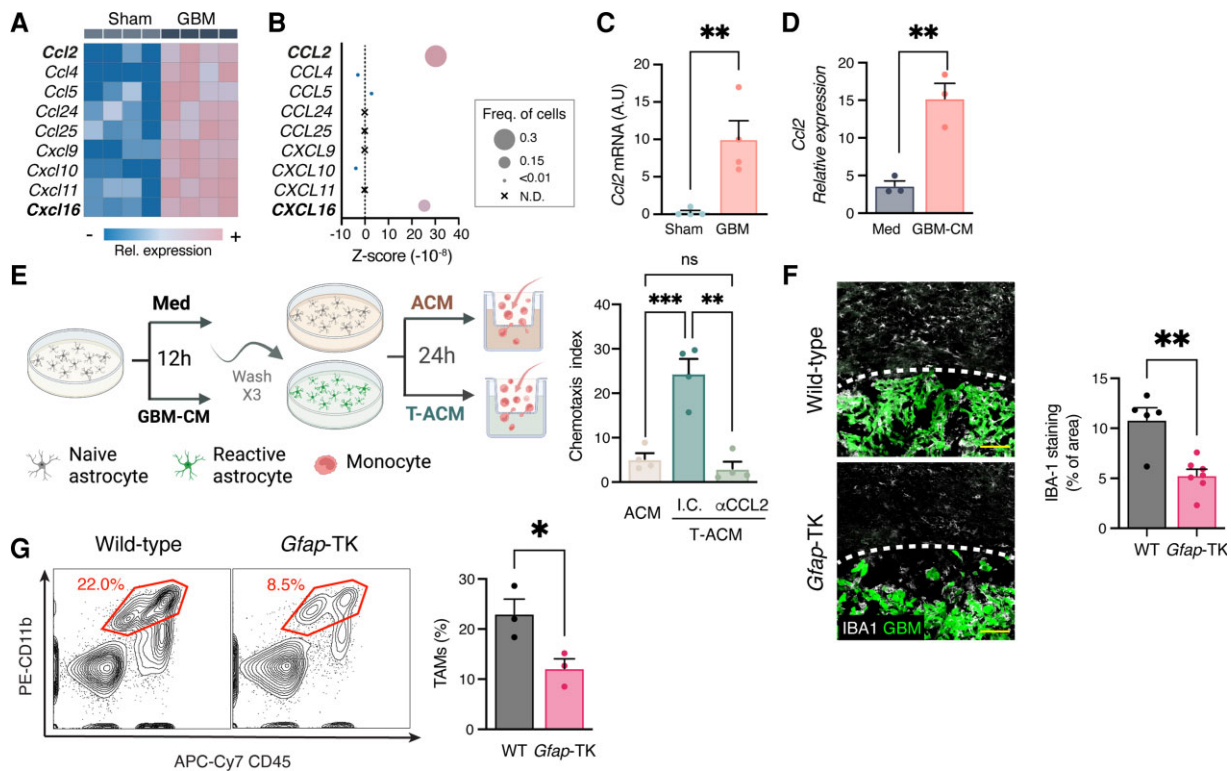


**Figure 3** TAA depletion attenuates TAM recruitment. (A–C) Chemokine expression in TAA. (A) Heat map of differently expressed chemokines (at least 2-fold,  $P_{adj} < 0.01$ ) (A) and *Ccl2* mRNA expression (C) in astrocytes derived from sham-injected or GBM-bearing mice, as in Fig. 2E. Data are representative of three independent experiments with  $n=4$  biologically independent samples. (B) scRNAseq analysis of chemokine expression intensity (colour-coded), frequency (dot size) and Z-score in TAAs from GBM patients<sup>42</sup> (astrocyte cluster as in Supplementary Fig. 2A). Expression levels (A and B) are defined by colour-coded expression as indicated (from blue to pink). (D) Primary astrocytes were stimulated with complete medium (Med) or GBM-CM from GL261 cells for 6 h. qPCR analysis of *Ccl2* expression normalized to *Ppia* ( $n=4$  biologically independent experiments). (E) Astrocytes were stimulated with complete medium or GBM-CM for 12 h, extensively washed and used to prepare ACM or tumour cell-induced ACM (T-ACM), which was tested in an *in vitro* monocyte migration assay. (F and G) Analysis of TAMs in the TME. GFP<sup>+</sup>-GL261 glioma cells were intracranially injected into wild-type (WT) or *Gfap*-TK mice. Following tumour establishment (Day 9 after tumour implantation), mice were treated daily with GCV (as in Fig. 1); TAMs recruitment to the tumour was examined 17 days after tumour implantation. (F) Representative immunofluorescence images TAMs stained for IBA-1 (white) in the tumour (GBM, green) microenvironment ( $n=2$  biologically independent experiments, four mice per group). Scale bars = 100  $\mu$ m. (G) Percentage of TAMs (CD11b<sup>+</sup> CD45<sup>+</sup>) gated from GCV-treated GL261-bearing wild-type and *Gfap*-TK mice. Representative flow cytometry plots from each group are shown on the left and quantification analyses are on the right ( $n=3$  independent experiments, six mice per experiment). Data are shown as mean  $\pm$  SEM. P-values were determined by one-way ANOVA, followed by Fisher's LSD *post hoc* analysis (E) or two-sided Student's *t*-tests (C, D, F and G). \* $P < 0.05$ , \*\* $P < 0.01$ , \*\*\* $P < 0.001$ .

for astrocyte modulation of microglial activity. The astrocytes were then removed by mild trypsin/EDTA treatment, and the microglial cells were co-incubated with GFP<sup>+</sup>-GL261 cells for 48 h. Glioma cells were then isolated on the basis of their green fluorescent protein (GFP) expression, and their viability was determined (as illustrated in Fig. 4G). We found that astrocytes attenuate the microglial-dependent killing of glioma cells by  $48 \pm 12.6\%$  (Fig. 4H). Next, we investigated whether this immunosuppressive function on microglial cell cytotoxicity towards glioma cells is a specific immunosuppression response or a general response to the withdrawal of trophic support by astrocytes. To this end, microglial cells were treated with ACM, which was generated from astrocyte cultures without previous contact with neither glioblastoma nor microglial cells, or control medium (Med) and co-incubated with GFP<sup>+</sup>-GL261 cells as in Fig. 4H. We found that ACM did not significantly regulate the microglial-dependent killing of glioma cells ( $P = 0.678$  by two-sided Student's *t*-test, Supplementary Fig. 5G). Suggesting that astrocytes play a direct and specific immunosuppressive function in regulating the microglial response to glioma cells. To continue and explore this hypothesis, we then repeated

in the presence of the NO synthase inhibitor, L-NAME, which has been shown to inhibit iNOS-depend neuroinflammation and microglial-induced cell death.<sup>72,73</sup> We observed that inhibition of NO synthesis also attenuates microglial-induced killing in our system, suggesting that it is at least partially dependent on NO production (Fig. 4I). Accordingly, we could also detect a significant upregulation in *Nos2* (the transcript encoding iNOS) expression in microglial cells isolated from GCV-treated GL261-bearing *Gfap*-TK, compared to wild-type mice (Fig. 4J). Next, we studied the signalling cascade by which astrocytes govern microglial reprogramming. Treating mixed glia cultures (containing microglial cells and astrocytes) with neutralizing antibodies to CSF1, TGF $\beta$ , IL-10, IFN $\gamma$  or IL-6 signalling, and analysing GBM-CM stimulated microglial induction of *Nos2*, indicated that blockade of CSF-1R induced its expression. Suggesting that astrocyte-driven CSF1 inhibits microglial *Nos2* induction (Fig. 4K). Of note, blocking CSF-1R signalling did not significantly regulate microglial viability or microglial proliferation (Supplementary Fig. 5H and I). Indeed, analysis of TCGA data, and scRNAseq data of the GBM TME,<sup>42</sup> identify the upregulation of CSF1 and CSF-1R expression (mainly in astrocytes and TAMs,

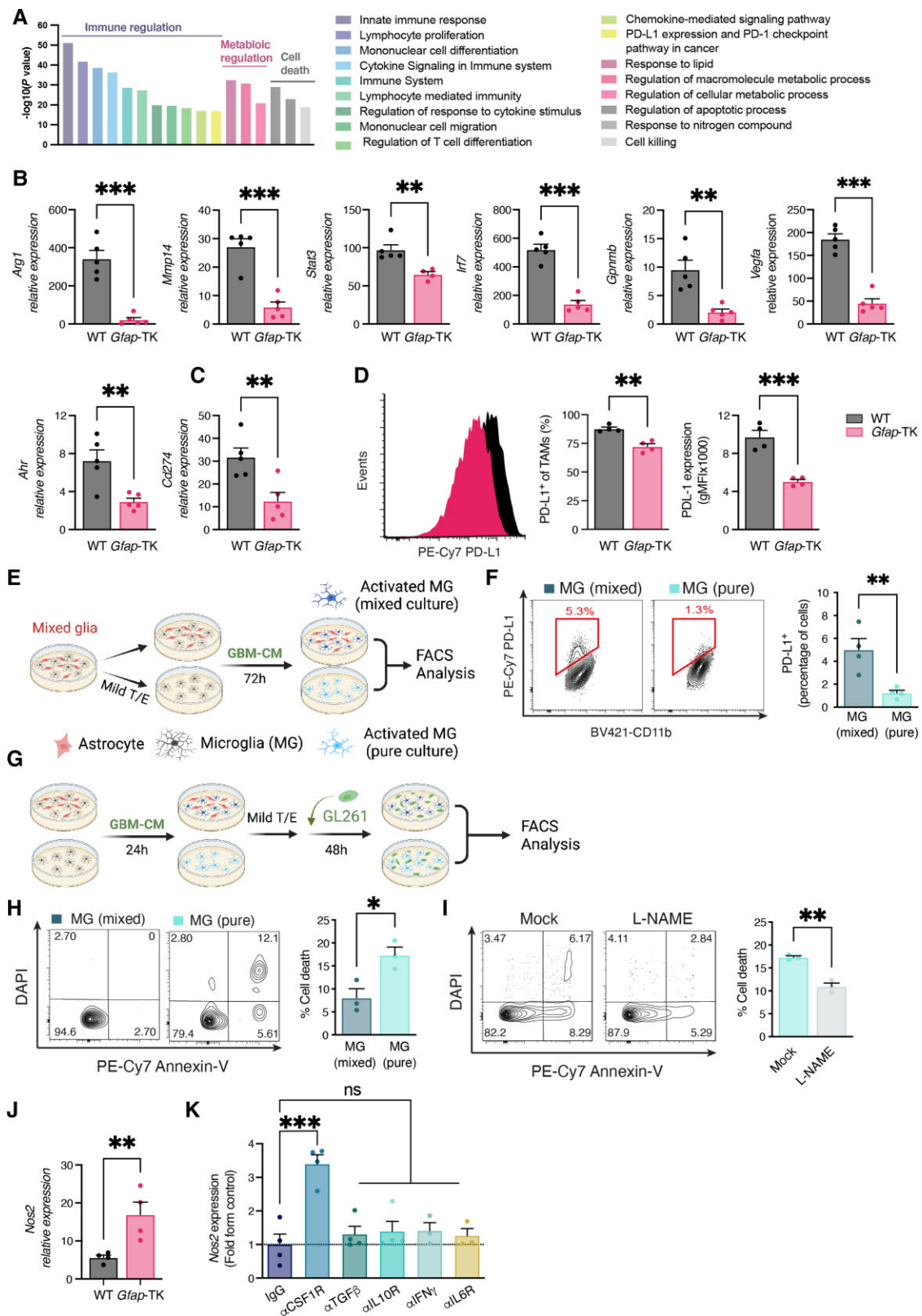


**Figure 4** TAA ablation attenuates TAM activation. (A–D) Functional analysis of TAMs (CD11b<sup>+</sup>CD45<sup>+</sup>) isolated from GCV-treated wild-type (WT) and *Gfap-TK* GL261-implanted mice (as in Fig. 3) 17 days after tumour implantation. (A) Pathway enrichment analysis of differentially expressed genes (at least 2-fold,  $P_{adj} < 0.05$ ) as detected by Nanostring (Supplementary Fig. 5A). (B and C) qPCR analysis of *Arg1*, *Ahr*, *Stat3*, *Irf7*, *Gpmb*, *Vegfa*, *Mmp14* and *Cd274* expression in FACS-sorted TAMs; expression normalized to *Ppia*. Data are representative of three independent experiments ( $n=4$  biologically independent samples, pool of two mice per sample). (D) PD-L1 expression in TAMs. Representative flow cytometry plots from

(Continued)

respectively), which is correlated with lower patient survival (Supplementary Fig. 5J–N). Taken together, the data indicate that astrocytes reprogramme the microglial cells to promote immunosuppression and support tumour survival, a process that is partly mediated by CSF1 signalling and iNOS expression.

### Astrocyte-derived cholesterol supports glioma survival

The metabolism of cancer cells adapts during transformation, and the altered cellular metabolism that is a hallmark of gliomas, may be a promising source of druggable targets for therapy.<sup>2,74</sup> This is particularly pertinent for glioblastoma progression, as the CNS is isolated from the circulation by the blood–brain barrier and depends heavily on astrocytes for metabolic homeostasis. Our analysis of the tumour-associated astrocyte transcriptome suggests a significant perturbation in the metabolic network (Fig. 2F). We used genome-scale metabolic modelling<sup>31</sup> to identify which of the astrocyte core metabolic pathways are regulated by the tumour, since this method was previously shown to model human brain metabolism in health and disease.<sup>75,76</sup> For this purpose, we analysed the transcriptome data using the Integrative Metabolic Analysis Tool (iMAT<sup>31</sup>) to predict the metabolic flux activity (Table 1). Interestingly, the results reveal a significant enrichment of the cholesterol metabolic pathway ( $P = 1.22 \times 10^{-15}$ ).

Cholesterol is predominantly localized to bilayer membranes such as the cell membrane and the mitochondrial membrane. It is essential for cellular biological functions ranging from signal transduction to modulation of critical mitochondrial-governed processes such as oxidative phosphorylation (OXPHOS) and regulation of apoptosis.<sup>77,78–79</sup> Many cancers display a high cholesterol content, which is thought to support tumour growth<sup>29,79,80</sup> and the viability and activity of cells in the TME,<sup>29</sup> and targeted disruption of cholesterol metabolism was recently shown to be beneficial in adult and childhood brain tumours.<sup>26,81</sup> Analysis of cholesterol distribution in the brain of GL261-bearing mice identified higher cholesterol levels in the tumour cells than in the surrounding brain tissue, which agrees with previous reports<sup>2,26</sup> that glioma cells take up significantly more extracellular cholesterol than non-neoplastic cells (Supplementary Fig. 6A). Importantly, cholesterol synthesis in the brain is mainly dependent on astrocytes, as the blood–brain barrier effectively prevents the uptake of lipoprotein-bound cholesterol from circulation. Indeed, perturbations in astrocyte-derived cholesterol have been associated with a variety of neuropathologies.<sup>22,82</sup> However, the role of astrocyte-derived cholesterol in GBM progression is unknown.

Since cholesterol has been found to be specifically enriched in the mitochondrial membrane of cancer cells where it decreases membrane fluidity and reduces the mitochondria sensitivity to stress,<sup>79,83</sup> we hypothesized that cholesterol produced by the TAAs could be used to regulate GBM pathogenicity. To test this hypothesis, we first studied the dependency of glioma cells on exogenous cholesterol by removing the cholesterol-carrying lipoproteins from the culture media and assessing the mitochondrial bioenergetic potential as an indication of cellular stress. Interestingly, although like many other cancer cells glioma cells can use glycolysis for growth (Warburg effect), they rely on mitochondrial OXPHOS to support aggressive tumour growth.<sup>2,4</sup> We therefore monitored the ECAR, indicative of aerobic glycolysis and oxygen consumption rate (OCR) as a readout of OXPHOS, in GL261 and CT-2A glioma cells cultured for 18 h in media supplemented with LPDS or normal serum (FCS) (Fig. 5A and B and Supplementary Fig. 6B and C). We found that lipoprotein depletion had little to no effect on ECAR, and the addition of glucose did not affect the cytosolic-based glycolysis rate or glycolytic capacity in the glioma cell lines, with only a minor effect on the GL261 glycolytic reserve (Fig. 5A and Supplementary Fig. 6B). However, in absence of lipoproteins, there was significant inhibition of the OCR potential as well as a decrease in basal respiration and ATP production by the glioma cells. Notably, OCR was attenuated when oxygen consumption was uncoupled from ATP production by FCCP [carbonyl cyanide4-(trifluoromethoxy)phenylhydrazone], demonstrating a significant reduction in the glioma cells' maximal respiration and spare respiratory capacity. Thus, suggesting that the removal of exogenous cholesterol resulted in mitochondrial stress, specifically targeting the OCR activity of the glioma cells, which is required for the tumour progression.<sup>3,4</sup>

Mitochondrial stress is often associated with cell death, as is the reduction in cellular cholesterol levels.<sup>79,83</sup> Therefore, we analysed the viability of the murine glioma cells and primary astrocytes subjected to prolonged deprivation of cholesterol. We reasoned that while astrocytes, which can *de novo* synthesize cholesterol, will resist exogenous cholesterol deprivation, the murine glioma cells will be highly vulnerable. To address this objective, we treated primary astrocytes and glioma cells with lovastatin, which inhibits the 3-hydroxy-3-methylglutaryl-CoA reductase (HMGCR), a rate-limiting enzyme in the cholesterol synthesis pathway. We found that suppressing endogenous cholesterol synthesis did not affect glioma viability, but led to significant cell death of primary astrocytes (Supplementary Fig. 6D and E). Conversely, depriving the murine glioma cells of lipoprotein-bound cholesterol resulted in substantial cell death while astrocyte viability remained unaffected

#### Figure 4 Continued

each group are shown on the left and quantification analyses of the percentage of PD-L1<sup>+</sup> TAMs and PD-L1 expression (geometric mean fluorescence intensity, gMFI) is on the right. Data are representative of three independent experiments ( $n = 4$  biologically independent samples, pool of two mice per sample). (E and F) Mixed glial cultures were treated with mild trypsin/EDTA to remove the astrocyte monolayer leaving only the microglia attached to the plate, or were left untreated. Cultures were then treated with GL261 conditioned media (GBM-CM) for 72 h. (F) Representative flow cytometry plots of microglial (gated as CD11b<sup>+</sup> cells) PD-L1 expression from each group are shown on the left, and quantification analyses of the percentage of PD-L1<sup>+</sup> microglial cells are on the right ( $n = 4$  biologically independent experiments). (G) Mixed glia and microglial cultures were prepared as in E and treated with GBM-CM for 24 h. Microglial cultures were then isolated with mild trypsin/EDTA and co-cultured with GFP<sup>+</sup>-GL261 cells for 48 h. The viability of GFP-gated GL261 cells was then determined by Annexin-V assay. (H) Representative flow cytometry plots of GFP-gated GL261 cells from each group are shown on the left, and quantification analyses of cell death are on the right ( $n = 4$  biologically independent experiments). (I) Microglial cultures were pretreated with L-NAME (2 mM) before co-incubation with GL261 cells, and glioma viability was analysed as in H.  $n = 3$  biologically independent experiments. (J) qPCR analysis of *Nos2* expression in FACS-sorted microglial cells (CD11b<sup>+</sup>CD45<sup>dim</sup>) isolated from GCV-treated wild-type and *Gfap*-TK GBM-bearing mice, as in Fig. 1; expression normalized to *Ppia*. Data are representative of three independent experiments ( $n = 3$  biologically independent samples, pool of two mice per sample). (K) Mixed glial cells were treated with the indicated blocking antibodies or appropriate isotype controls (25 µg/ml), and then activated with GBM-CM. Microglia were isolated as in E, and microglial expression of *Nos2* was determined by qPCR relative to *Ppia* ( $n = 5$  biologically independent experiments). Data are shown as mean  $\pm$  SEM. *P*-values were determined by two-sided Student's *t*-tests (A–J) and one-way ANOVA, followed by Fisher's LSD *post hoc* analysis (K) or \* $P < 0.05$ , \*\* $P < 0.01$ , \*\*\* $P < 0.001$ ; ns = not significant.

**Table 1 Metabolic pathway enrichment in glioblastoma-associated astrocytes**

Metabolic pathway	P-value
Bile acid biosynthesis	$<10^{-16}$
Hyaluronan metabolism	$<10^{-16}$
Stilbene, coumarine and lignin biosynthesis	$<10^{-16}$
Cholesterol metabolism	$1.22 \times 10^{-15}$
Folate metabolism	$4.04 \times 10^{-7}$
Ubiquinone biosynthesis	$3.88 \times 10^{-6}$
Carnitine shuttle	$1.83 \times 10^{-5}$
Eicosanoid metabolism	$7.21 \times 10^{-5}$
Transport, lysosomal	$1.13 \times 10^{-4}$
Transport, peroxisomal	$3.72 \times 10^{-4}$
Transport, endoplasmic reticular	$3.91 \times 10^{-4}$
Pentose and glucuronate interconversions	$3.85 \times 10^{-3}$
Nucleotide sugar metabolism	$6.69 \times 10^{-3}$
Glycosylphosphatidylinositol-anchor biosynthesis	$6.82 \times 10^{-3}$

(Fig. 5C), suggesting that the glioma cells are indeed dependent on exogenous cholesterol. Consistent with this interpretation, removing the cholesterol-carrying lipoproteins from the culture media increased the expression of the LDLR, which mediates cholesterol uptake by the cells, a finding we have also noted in GBM patients (Supplementary Fig. 6F and G). Furthermore, exogenous cholesterol overcame the deleterious effects of lipoprotein-bound cholesterol deprivation on glioma viability (Fig. 5D). Also, similarly, activating the liver X receptor (LXR) signalling pathway with the endogenous ligand 24(S)-hydroxycholesterol (24-OHC), which results in a 24-OHC dose-dependent LDLR degradation, thus limiting cholesterol uptake by the cells,<sup>26</sup> led to dramatic cell death in both GL261 and CT-2A glioma cell lines (Fig. 5E and F). Collectively, these data demonstrate that glioma cells depend on exogenous cholesterol for their survival. Importantly, these findings align with similar data described recently by Villa *et al.*<sup>26</sup> that demonstrate a dependency of human gliomas on LXR-dependent cholesterol uptake.

Next, we investigated the dynamics of cholesterol metabolism in the astrocyte-glioma cross-talk. Treating astrocytes with GBM-CM, or co-culturing them with glioma cells, induces the expression of rate-limiting enzymes in the cholesterol *de novo* synthesis pathway, including *Hmgcs1*, *Hmgcr* and *Dhcr24* (Supplementary Fig. 7A–C). Again, this increase is in line with the elevated expression levels of these genes seen in scRNAseq data of astrocytes from GBM patients<sup>42</sup> (Supplementary Fig. 7D), suggesting that glioma cells may elicit astrocytes to support their metabolic requirement for cholesterol. Culturing glioma cells in the presence (co-culture) or absence (mono-culture) of astrocytes, and subjecting them to lipoprotein deprivation, revealed a dramatic rescue of the murine GL261 and CT-2A glioma cells by the astrocytes (Fig. 5G and Supplementary Fig. 7E). Moreover, we found a similar recovery from cholesterol starvation in human U87EGFRvIII<sup>26</sup> glioma cells in the presence of human primary astrocytes (Fig. 5H and Supplementary Fig. 7F). Taken together, these data indicate that the glioma cells rely on the uptake of exogenous cholesterol for survival and that human and murine astrocytes can meet these metabolic requirements for cholesterol and support glioma cell survival.

### Astrocytic ABCA1-driven cholesterol efflux promotes tumour progression

Intracellular cholesterol trafficking in the brain is mediated mainly by the sterol transporters ABCA1 (ATP binding cassette transporter

A1) and ABCG1 (ATP binding cassette subfamily G member 1).<sup>84</sup> Our analysis of TCGA data identified a high expression of both genes in the CNS of GBM patients (Fig. 6A and Supplementary Fig. 8A), although our analysis of scRNAseq of the GBM microenvironment<sup>42</sup> identified that TAAs predominantly express ABCA1 (Fig. 6B). Transcriptomic analysis of the TAAs isolated from GBM-bearing mice transcriptome similarly detected high levels of *Abca1* induction with an absence of *Abcg1* transcripts (Fig. 6C). Concomitantly, we could detect the expression of ABCA1 in reactive astrocytes surrounding the GBM tumour in mice by immunofluorescence (Fig. 6D) and also show that exposure to GBM-CM directly induces ABCA1 expression in astrocytes (Fig. 6E), suggesting that ABCA1 plays a role in the astrocyte-mediated cholesterol shuttling to the tumour.

We, therefore, reasoned that knocking down astrocytic ABCA1 expression would limit the astrocyte-derived cholesterol available to the tumour cells and enable us to evaluate the extent to which it contributes to tumour pathology. To investigate this hypothesis, we generated ABCA1-targeting lentiviruses using RNA interference (RNAi) or the CRISPR–Cas9 systems (Fig. 6F and Supplementary Fig. 8B, respectively). We transduced primary astrocytes with our lentiviruses targeting ABCA1 [shAbca1, sgAbca1(#1) and sgAbca1(#2)] or appropriate controls [non-targeting shRNA (shNT) or sgRNA targeting the luciferase gene (sgLuc2), respectively]. We found that all *Abca1*-targeting sequences significantly knocked-down ABCA1 expression compared to their respective controls (Supplementary Fig. 8C). We next studied whether astrocytic ABCA1 knock-down would attenuate astrocyte-mediated rescue of glioblastoma cells from cholesterol depredation. To that end, the transduced primary astrocytes were co-cultured with glioblastoma cells in a cholesterol-free medium, and their survival was analysed (as in Fig. 5G). We found that all *Abca1*-targeting sequences significantly inhibited the astrocyte-mediated rescue of the glioma cells (Supplementary Fig. 8D). Thus, these data demonstrate that ABCA1 plays an important role in the astrocyte-mediated cholesterol shuttling to the glioma cells.

To further investigate our initial hypothesis and determine the role of astrocytic ABCA1 expression on tumour pathogenicity, we delivered the validated shRNAs (shAbca1 or shNT) to reactive astrocytes in the GBM TME. To this end, we used a previously established lentivirus-based system optimized for astrocyte-specific knock-down *in vivo*<sup>19,21,23</sup> (Fig. 6F). In this system, the truncated GFAP promoter, GfaABC1D, drives the expression of a miR30-based shRNA and a GFP reporter. Intracranial injection of shRNA-encoding lentivirus to GL261-bearing mice indeed confirmed that the GFP reporter was detected exclusively in the GFAP<sup>+</sup> astrocytes (Supplementary Fig. 8E and F), and significantly reduced astrocytic *Abca1* expression (Fig. 6G).

As the next step, we investigated whether knock-down of *Abca1* in astrocytes affects the cholesterol content of tumour cells. To address this objective, GL261-bearing mice were intracranially injected with the *Gfap*-shNT or *Gfap*-shAbca1 and we assessed cholesterol accumulation in the tumour cells using Filipin III staining.<sup>29</sup> In accordance with our hypothesis, knock-down of astrocytic *Abca1* led to a significant decrease in glioma cholesterol (Fig. 6H) and concomitant induction of apoptotic cell death (Fig. 6I). Moreover, inhibiting the efflux of cholesterol from the TAAs significantly regressed tumour growth and prolonged survival of the GL261-bearing mice (Fig. 6J and K). Notably, analysis of TCGA data indicated that reduced expression of ABCA1 was associated with increased survival in patients with GBM (Fig. 6L). Collectively, these data suggest that glioblastoma pathogenicity is dependent on astrocyte-derived cholesterol.

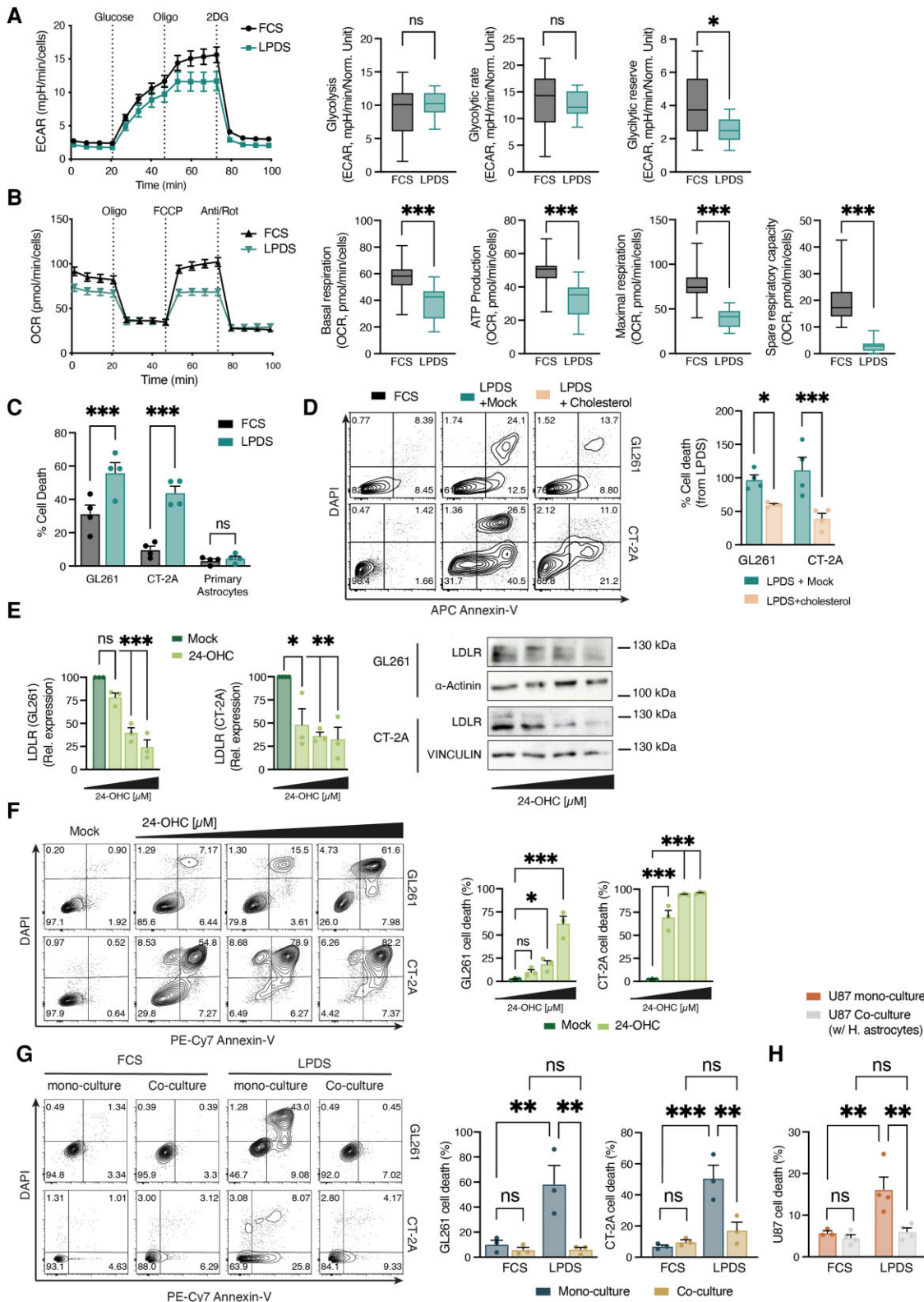


**Figure 5 Astrocyte-derived cholesterol support glioma survival.** (A and B) Real-time changes in the ECAR (A) and OCR (B) of GL261 glioma cells, cultured in media supplemented with full serum (FCS) or lipoprotein-deprived serum (LPDS) for 18 h and measured using Seahorse. Oligo = oligomycin; FCCP = carbonyl cyanide4-(trifluoromethoxy) phenylhydrazone; R/A = rotenone plus antimycin A; 2-DG = 2-deoxy-D-glucose. Glycolysis, glycolytic capacity and glycolytic reserve were extracted from the ECAR reading, and basal respiration, ATP production, maximal respiration and spare respiratory capacity were determined on the basis of OCR. Data are representative of two independent experiments (n=6 technical replicates per experiment). (C) Percentage of cell death of GL261 and CT-2A glioma cells, or primary astrocytes, cultured in FCS or LPDS for 5 days; as determined by Annexin-V assay (n=4 independent experiments). (D) GL261 or CT-2A glioma cells were cultured in FCS or LPDS-media and treated with PBS (Mock) or

(Continued)

## Discussion

Whereas it is becoming increasingly clear that astrocytes play an important role in a number of neurological disorders, little is known about the nature of astrocyte contribution to glioblastoma pathogenicity *in vivo*. Here, we first addressed this question by genetically depleting GFAP<sup>high</sup> reactive astrocytes in adult immunocompetent mice, a method that has proven valuable for understanding the role of astrocytes in various neuropathologies.<sup>19,28,48,49</sup> Two models were used: the *Gfap*Cre:iDTR mice model, which depletes GFAP<sup>high</sup> astrocytes, and the *Gfap*-TK mice model,<sup>19,48,49</sup> which also requires the astrocytes to be in a proliferative state [a characteristic feature of both human<sup>24</sup> and murine TAAs (Fig. 2E and F)]. The results indicate that ablation of reactive glioma-associated astrocytes from the TME halts tumour progression, regresses established gliomas and markedly enhances survival of the animals in both GBM models (Fig. 1 and Supplementary Fig. 1), suggesting that TAAs play a pivotal role in controlling glioblastoma pathogenicity.

To unravel the molecular circuits by which astrocytes govern GBM pathogenicity, we performed RiboTag-based RNA-seq on TAAs. RiboTag restricts analysis to ribosome-associated mRNAs that are likely to be in active translation, thereby reflecting the cellular protein expression profile, while minimizing any bias resulting from cell isolation-based methods.<sup>85,86</sup> Our results identify unique transcriptomic reprogramming of glioma-associated astrocytes, with the capacity to directly induce immunosuppression and control the immunological compartment and the metabolic landscape of the TME (Fig. 2 and Supplementary Fig. 2). Importantly, our astrocyte gene expression dataset is validated by broad agreement with other RNA-seq profiles of astrocytes from the GBM patients including the scRNAseq analysis of the GBM (IDH1-negative, grade IV) TME by Darmanis *et al.*<sup>42</sup> and the analysis of GBM-associated astrocytes isolated by immunopanning by Henrik Heiland *et al.*<sup>24</sup>

TAMs, which possess both tumour-promoting and immunosuppressive capacities, are abundant in the TME. Since their accumulation has been shown to be reversely correlated with patient survival, and given the abysmal prognosis of GBM patients, there is growing interest in developing novel therapeutics to target TAM activity. However, whether these activities are predominantly shaped by the non-neoplastic cells in the TME milieu or by the malignancy itself is unknown.<sup>87</sup> Here we demonstrate that astrocytes have an important role in reprogramming TAMs in the glioma microenvironment. We found that astrocytes regulate the recruitment of TAMs to the tumour (Fig. 3) and control various aspects of the TAM tumour-promoting and immunosuppressive phenotype (Fig. 4 and Supplementary Fig. 5). In addition, we implicate the CCL2–CCR2 and CSF1–CSF1R axes in the molecular mechanisms by which the astrocytes control the TAM compartment and thus shape tumour-specific immunity (Figs 3 and 4). We could also detect an increased expression of these genes in GBM patient-derived

scRNAseq and in TCGA data, which was inversely correlated to patient survival (Supplementary Figs 4 and 5). Similar expression and survival patterns were also found for CD274, the transcript encoding PD-L1 (Supplementary Fig. 5). These findings are in agreement with previous reports showing the perturbations of CCL2, CSF1 or PD-L1 signalling are able to regulate the TAMs niche in the TME and affect tumour pathogenicity in mouse models of GBM.<sup>7,52,88</sup> Regulating TAMs activity, for example, by using minocycline that blocks microglial activation or the specific CSF-1R inhibitor PLX3397, reduces glioma expansion in experimental glioma mouse models. Unfortunately, so far, the clinical application of these basic science advances has been disappointing, and strategies designed to silence TAM function have not translated well to human clinical trials.<sup>57,89</sup> Immunotherapies have demonstrated limited efficacy in patients with glioblastoma. However, in recent early phase clinical trials, the use of nivolumab or pembrolizumab, which targets the PD-L1/PD-1 axis, has shown promising outcomes.<sup>10,14</sup> Thus, suggesting that to overcome the tumour-supporting properties of the TAMs, it might not be enough to target specific aspects of TAM biology. Instead, there is a need to develop strategies to harness the astrocytes to reprogramme the TAMs and redirect them back to fight cancer.

Alterations in cellular metabolism, governed by the interaction between tumour genotype and its microenvironment, are a hallmark of many malignancies including brain gliomas.<sup>2</sup> Cancer cells, due to their genetic abnormalities, aggressive proliferation rate and metabolic restrictions of their microenvironment, may become dependent on factors that are not themselves oncogenic. This process is known as non-oncogene addiction or non-oncogene co-dependency and opens up treatment possibilities. Accordingly, two of the main genetic abnormalities found in GBM tumours are the amplification of the gene encoding for epidermal growth factor receptor (EGFR), with nearly half of the cases bearing the gain-of-function EGFR variant III (EGFRvIII) alteration; And, the recurrence of mutations in the genes *IDH1* and *IDH2*, which are components involved in the tricarboxylic acid cycle. Both EGFR and *IDH* have been associated with the regulation of glioma bioenergetics, which favours OXPHOS for aggressive growth, over glycolysis.<sup>2,4</sup> Accordingly, treatment of patient-derived GBM xenograft mice with Gboxin, an OXPHOS inhibitor, suppresses the growth of tumours with EGFR or *IDH1* mutations.<sup>3</sup> In recent years, several important findings as to the role of *IDH* mutations in glioblastoma pathogenicity, have linked tumour metabolism and immune perturbations of T cells<sup>87,90</sup> and TAMs<sup>58,87</sup> in TME. Accordingly, Bunse *et al.*<sup>90</sup> have elegantly demonstrated that the oncometabolite (R)-2-hydroxyglutarate, produced by *IDH* mutations, suppresses T-cell activity, while Klemm *et al.*<sup>58</sup> found that *IDH* mutation status shapes TAM composition (favouring microglial recruitment over monocyte-derived macrophages) and phenotype (e.g. suppressing GPNMB induction) in TME, suggesting that understanding the immunometabolic cross-talk between the glioma cells and the non-neoplastic cells in the TME is becoming increasingly important

### Figure 5 Continued

cholesterol (250 ng/ml) for 5 days. Representative flow cytometry plots of Annexin-V/DAPI staining from each group are shown on the left and quantification analyses of cholesterol rescue are on the right ( $n = 4$  biologically independent experiments). (E and F) Representative images and quantification of LDLR expression (Immunoblot, E) and cell death via FACS analysis of Annexin-V/DAPI staining (F) in response to endogenous LXR agonists (24-OHC) or Mock (DMSO) treatment in GL261 and CT-2A cells. ( $n = 3$  biologically independent experiments). (G and H) Analysis of LPDS-induced glioma cell death, in the presence of absence of primary astrocytes, by Annexin-V assay. (G) Representative flow cytometry plots of murine GL261 and CT-2A glioma cells co-cultured for 5 days with primary mouse astrocytes are shown on the left and quantification analyses on the right ( $n = 4$  biologically independent experiments). (H) quantification analyses of human U87EGFRvIII<sup>26</sup> (U87) glioma cells co-cultured with human primary astrocytes for 5 days ( $n = 3$  biologically independent experiments). Data are shown as mean  $\pm$  SEM. P-values were determined by two-sided Student's t-tests (B–D, G and H) or by two-way ANOVA (E and F). \* $P < 0.05$ , \*\* $P < 0.01$ , \*\*\* $P < 0.001$ .

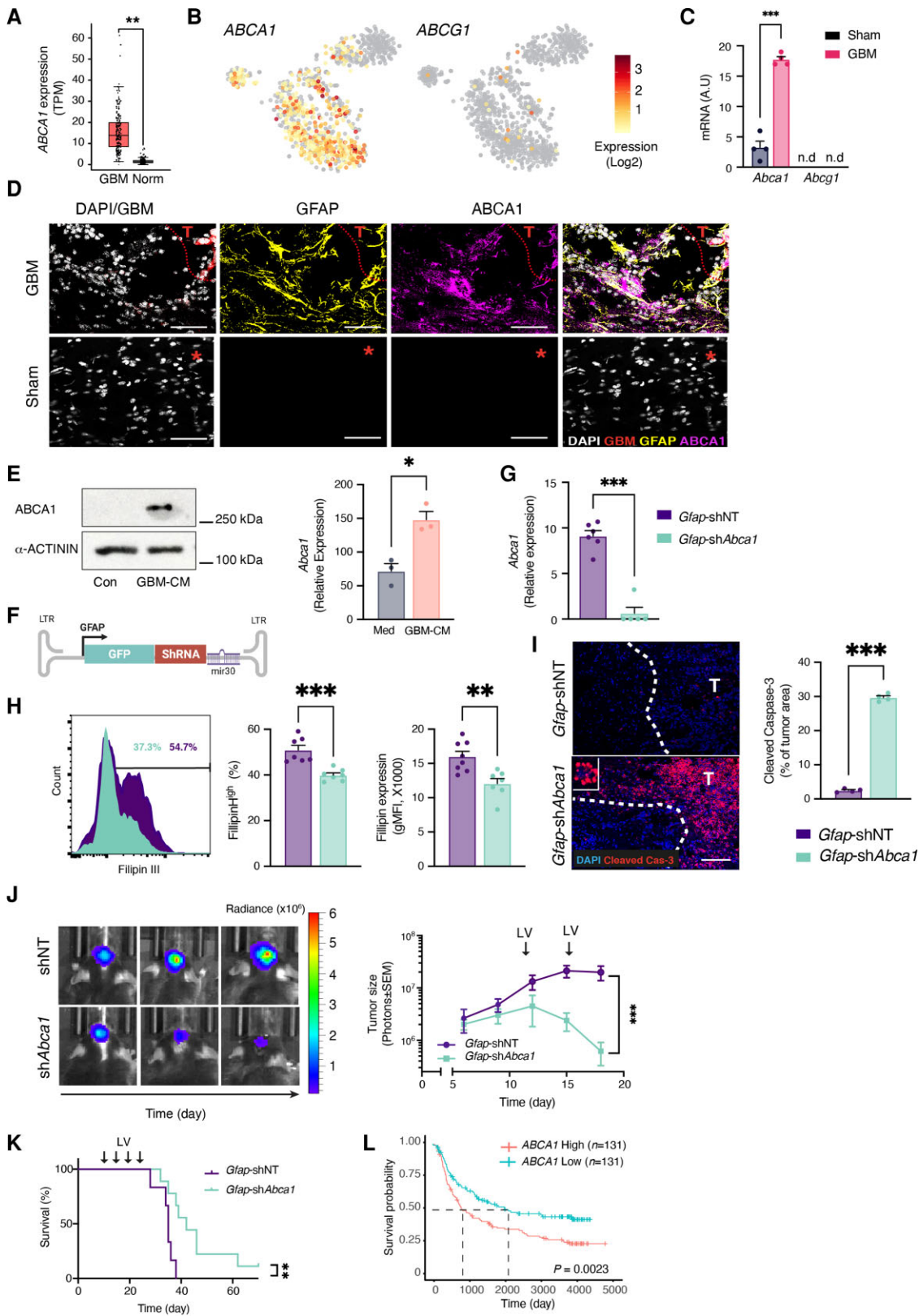


**Figure 6** Astrocytic expression of ABCA1 regulates glioma cholesterol levels and tumour progression. (A) Box plot analysis of TCGA gene expression for ABCA1 in normal (Norm; n=207) or GBM patients (n=163). n represents the number of patients per group. (B) Heat map overlay of the scRNAseq gene expression intensity of ABCA1, and ABCG1 in TAAs from GBM patients<sup>42</sup> (astrocyte cluster as in Supplementary Fig. 3A). (C) qPCR analysis of *Abca1* expression in Ribotag-isolated astrocytes GBM-bearing mice, as in Fig. 2. (D) Representative immunofluorescence images of sham-injected or GL261-bearing mice stained for ABCA1 (purple), GFAP (reactive astrocytes, yellow), GBM (GFP<sup>+</sup>-GL261, red) and nuclei (DAPI, white); asterisk indicates the injection coordinates in sham, scale bars = 35 μm (n=2 biologically independent experiments, four mice per group).

(Continued)



for finding more effective ways to treat glioblastoma patients: specifically, by targeting the tumour altered cellular metabolism, and the unique metabolic vulnerabilities enforced by the blood–brain barrier. However, currently, the metabolic landscape of the GBM microenvironment and the mechanisms by which it is changed by the cross-talk between the glioma cells and the non-neoplastic cells in the TME, mainly the astrocytes, are not well understood.

We found that GBM modulates the metabolic activity of the TAAs and, using genome-scale metabolic network analysis, identified significant perturbations in several key metabolic pathways that might be associated with tumour progression. These include cholesterol metabolism,<sup>5,80</sup> bile acid (synthesized from cholesterol) biosynthesis and hyaluronan metabolism, which was shown to maintain the glioblastoma stem-like cell tumorigenicity potential<sup>91</sup> (Fig. 2F and Table 1). Given the unique role of astrocytes in controlling brain cholesterol homeostasis,<sup>2,92</sup> here we decided to focus on studying the contribution of astrocyte-derived cholesterol to glioma pathogenicity. Our results indicate that glioma cells rely on exogenous cholesterol to maintain their energy metabolism and support viability. Accordingly, deprivation of cholesterol-carrying lipoproteins from their environment lowers the OXPPOS potential, which is important for tumour progression.<sup>3,4</sup> Indeed, a variety of OXPPOS-targeting drugs, including metformin, Gboxin and IACS-010759, were shown to inhibit glioma proliferation and induce cell death. In this context, metformin combined with temozolomide (standard-of-care chemotherapy for GBM patients) or radiotherapy is currently in clinical trials for glioma (NCT02780024, NCT03243851).<sup>2</sup> In addition, we demonstrate that both mouse and human glioma cells are dependent on cholesterol efflux from the astrocytes (Fig. 5 and Supplementary Figs 6 and 7), and that blocking the efflux of cholesterol from the astrocytes, by targeting astrocytic expression of the cholesterol transporter ABCA1, causes regression of tumour growth and prolongs mouse survival (Fig. 6). The physiological relevance of these findings to human disease is provided by scRNAseq data analysis of the TME of GBM patients, as well as TCGA data demonstrating an increased expression of astrocytic ABCA1 in the GBM TME and an inverse correlation with patient survival. Further support is provided by recent reports by Villa et al.<sup>26</sup> that targeting the ABCA1–LDLR axis, using a brain-penetrant LXR agonist, kills glioma cells and attenuates tumour pathogenicity in a GBM xenograft model.

Our data demonstrate a tissue context in which reactive astrocytes in the TME supply the metabolic requirements of tumour cells, thereby exposing vulnerabilities that merit clinical exploitation and contributing to the recently emerging line of research that demonstrates a profound astrocyte-mediated metabolic-

dependent regulation of neuro-pathologies.<sup>15,19–21–22</sup> Notably, here we only addressed the cholesterol node in the astrocyte–tumour cell axis within the vast complexities of the metabolic network that governs GBM pathogenicity. Future studies should continue to unmask the role of additional metabolic circuits in the TME (Table 1), and expand our understanding of the wider role of astrocyte-derived cholesterol in the TME (e.g.<sup>29</sup>).

Astrocytes' diverse functions in health and disease encompass a continuum of cellular states with the potential for plasticity and reprogramming.<sup>93,94</sup> Recent scRNAseq studies had provided valuable insights into basal<sup>95</sup> and reactive-astrocyte heterogeneity in neuroinflammation and neurodegeneration.<sup>96,97</sup> However, little is known about astrocyte heterogeneity in the GBM TME, and the underlying mechanisms driving it. To address the question of astrocyte diversity, we analysed the astrocyte scRNAseq data from the GBM patients<sup>42</sup> by means of differential expression, pathway analysis and transcription factors enrichment. We found that the astrocytes clustered into two main populations (Supplementary Fig. 3C–H and Supplementary Table 3). Cluster A (Blue, 599 cells), which is enriched with the immune response transcripts, and cluster B (Pink, 453 cells), enriched in genes associated with cholesterol synthesis and bioenergetics (Supplementary Fig. 3C–G). Interestingly, each cluster was also significantly (FDR < 0.001) enriched by a unique transcription factor signature. The transcripts encoding AHR, ATF3, SOCS3, PITX1, RELB and CRBPB were mainly associated with cluster A, while the transcripts encoding NFIA, HES6, HES1, SOX11, SOX15, TFDP2 and PPARGC1A were mainly associated with cluster B (Supplementary Fig. 3H). Notably, several transcripts encoding key transcription factors<sup>19,25,93</sup> such as STAT1, STAT3, NFATC3, SOX9 and IRF1 displayed a pan-astrocyte activation pattern and were evenly expressed between the two clusters (Supplementary Fig. 3H). Suggesting a heterogeneity in the astrocyte response to the GBM TME. Interestingly, Kambach et al.<sup>98</sup> suggested an inverse correlation between astrocyte cell density and their capacity for cholesterol synthesis. To study if the difference in astrocyte cell density may be related to the differential expression in cholesterol synthesis between the two clusters, we analysed the expression of fibroblast growth factor 2 (FGF2), whose expression is inhibited in high cell density in human astrocytes.<sup>99</sup> We found that FGF2 expression was strongly associated with cluster A, and had no significant correlation with any of the key cholesterol synthesis transcripts that were shown to be associated with astrocyte density<sup>98</sup> (Supplementary Fig. 3I and J, respectively). Suggesting that astrocyte cell density plays a role in TAAs responses in the TME. Indeed, with recent advances in the field of spatial transcriptomics,

#### Figure 6 Continued

(E) Representative immunoblot (left) and quantitative reverse transcription (right) analyses comparing ABCA1 levels in primary astrocytes treated with GBM-CM for 24 h (immunoblot) or 6 h (quantitative reverse transcription; expression normalized to *Ppia*) ( $n = 3$  biologically independent experiments). (F) Schematic map of the astrocyte-specific shRNA lentiviral vector. (G–K) Intracranially injection of astrocyte-specific shAbca1 lentivirus attenuates GBM progressions. Non-targeting (*Gfap-shNT*) or *Abca1*-targeting (*Gfap-shAbca1*) astrocyte-specific lentiviruses were injected into the TME of GL261-bearing mice every 5 days (as indicated) starting 9 days after tumour implantation. (G) Quantitative reverse transcription analysis of FACS-sorted GFP<sup>+</sup>-astrocytes for *Abca1* on Day 18; expression normalized to *Ppia*. Data are representative of two independent experiments ( $n = 4$  biologically independent samples). (H) Representative flow cytometry plots of Filipin III staining in tdTomato<sup>+</sup>-expression GL261 cells from each group are shown on the left and quantification analyses of the percentage of Filipin<sup>+</sup> GL261 cells and filipin intensity (gMFI) are on the right. Data are representative of two independent experiments ( $n = 4$  biologically independent samples per group). (I) Representative immunofluorescence images of cleaved caspase-3 (red) and nuclei (DAPI, blue) 10 days after lentivirus injection are shown on the left and quantification is on the right. T indicates the tumour. Data are representative of two independent experiments ( $n = 4$  biologically independent samples per group). (J) Representative images of GL261-derived bioluminescence from each group are shown on the left and quantification of tumour size on the right. Data are representative of three independent experiments with  $n = 6$  mice/group. (K) Kaplan–Meier curves assessing overall survival of these groups. Data are representative of two independent experiments with  $n = 6$  mice/group. (L) Kaplan–Meier curves assess the overall survival of GBM patients on the basis of ABCA1 expression;  $n$  represents the number of patients per group. Data are shown as mean  $\pm$  SEM.  $P$ -values were determined by two-sided Student's  $t$ -tests (A, C, E, G, H and I), two-way ANOVA (J) or log rank (Mantel–Cox) test (K and L). \* $P < 0.05$ , \*\* $P < 0.01$ , \*\*\* $P < 0.001$ . n.d. = not detected.

it will be interesting to further investigate astrocyte heterogeneity in the GBM to better target the astrocyte regulation of the TME.

In conclusion, we identified a mechanism by which astrocytes participate in the control of TAM immunity and sustain the metabolic landscape necessary for tumour survival. These findings shed new light on the pivotal role astrocytes play in promoting glioblastoma pathogenicity and the potential vulnerabilities caused by the tumour dependence on astrocyte immunometabolic support of the TME, thereby identifying candidate targets for therapeutic intervention.

## Funding

This work was supported by grants from the Israel Cancer Research Fund (ICRF, GA-16-1640), Uncle Kory Foundation, and the United States-Israel Binational Science Foundation (BSF, 2019197) to L.M.

## Competing interests

The authors report no competing interests.

## Supplementary material

Supplementary material is available at *Brain* online.

## References

- Quail DF, Joyce JA. Microenvironmental regulation of tumor progression and metastasis. *Nat Med*. 2013;19:1423–1437.
- Bi J, Chowdhry S, Wu S, Zhang W, Masui K, Mischel PS. Altered cellular metabolism in gliomas—An emerging landscape of actionable co-dependency targets. *Nat Rev Cancer*. 2020;20:57–70.
- Shi Y, Lim SK, Liang Q, et al. Gboxin is an oxidative phosphorylation inhibitor that targets glioblastoma. *Nature*. 2019;567:341–346.
- Marin-Valencia I, Yang C, Mashimo T, et al. Analysis of tumor metabolism reveals mitochondrial glucose oxidation in genetically diverse human glioblastomas in the mouse brain in vivo. *Cell Metab*. 2012;15:827–837.
- An Z, Weiss WA. Cholesterol: An Achilles' heel for glioblastoma? *Cancer Cell*. 2016;30:653–654.
- Kohanbash G, Carrera DA, Shrivastav S, et al. Isocitrate dehydrogenase mutations suppress STAT1 and CD8+ T cell accumulation in gliomas. *J Clin Invest*. 2017;127:1425–1437.
- Pyonteck SM, Akkari L, Schuhmacher AJ, et al. CSF-1R inhibition alters macrophage polarization and blocks glioma progression. *Nat Med*. 2013;19:1264–1272.
- Quail DF, Bowman RL, Akkari L, et al. The tumor microenvironment underlies acquired resistance to CSF-1R inhibition in gliomas. *Science*. 2016;352:aad3018.
- Takenaka MC, Gabriely G, Rothhammer V, et al. Control of tumor-associated macrophages and T cells in glioblastoma via AHR and CD39. *Nat Neurosci*. 2019;22:729–740.
- Cloughesy TF, Mochizuki AY, Orpilla JR, et al. Neoadjuvant anti-PD-1 immunotherapy promotes a survival benefit with intratumoral and systemic immune responses in recurrent glioblastoma. *Nat Med*. 2019;25:477–486.
- Sun C, Mezzadra R, Schumacher TN. Regulation and function of the PD-L1 checkpoint. *Immunity*. 2018;48:434–452.
- Ostrom QT, Gittleman H, Truitt G, Boscia A, Kruchko C, Barnholtz-Sloan JS. CBTRUS statistical report: Primary brain and other central nervous system tumors diagnosed in the United States in 2011–2015. *Neuro Oncol*. 2018;20:iv1–iv86.
- Wen PY, Reardon DA. Neuro-oncology in 2015: Progress in glioma diagnosis, classification and treatment. *Nat Rev Neurol*. 2016;12:69–70.
- Zhao J, Chen AX, Gartrell RD, et al. Immune and genomic correlates of response to anti-PD-1 immunotherapy in glioblastoma. *Nat Med*. 2019;25:462–469.
- Ferris HA, Perry RJ, Moreira GV, Shulman GI, Horton JD, Kahn CR. Loss of astrocyte cholesterol synthesis disrupts neuronal function and alters whole-body metabolism. *Proc Natl Acad Sci U S A*. 2017;114:1189–1194.
- Allen NJ, Eroglu C. Cell biology of astrocyte-synapse interactions. *Neuron*. 2017;96:697–708.
- Linnerbauer M, Wheeler MA, Quintana FJ. Astrocyte crosstalk in CNS inflammation. *Neuron*. 2020;108:608–622.
- Liddel SA, Barres BA. Reactive astrocytes: Production, function, and therapeutic potential. *Immunity*. 2017;46:957–967.
- Mayo L, Trauger SA, Blain M, et al. Regulation of astrocyte activation by glycolipids drives chronic CNS inflammation. *Nat Med*. 2014;20:1147–1156.
- Wheeler MA, Jaronen M, Covacu R, et al. Environmental control of astrocyte pathogenic activities in CNS inflammation. *Cell*. 2019;176:581–596.e18.
- Chao CC, Gutierrez-Vazquez C, Rothhammer V, et al. Metabolic control of astrocyte pathogenic activity via cPLA2-MAVS. *Cell*. 2019;179:1483–1498.e22.
- Wang H, Kulas JA, Wang C, Holtzman DM, Ferris HA, Hansen SB. Regulation of beta-amyloid production in neurons by astrocyte-derived cholesterol. *Proc Natl Acad Sci U S A*. 2021;118.
- Mayo L, Cunha AP, Madi A, et al. IL-10-dependent Tr1 cells attenuate astrocyte activation and ameliorate chronic central nervous system inflammation. *Brain*. 2016;139(Pt 7):1939–1957.
- Henrik Heiland D, Ravi VM, Behringer SP, et al. Tumor-associated reactive astrocytes aid the evolution of immunosuppressive environment in glioblastoma. *Nat Commun*. 2019;10:2541.
- Priego N, Zhu L, Monteiro C, et al. STAT3 labels a subpopulation of reactive astrocytes required for brain metastasis. *Nat Med*. 2018;24:1024–1035.
- Villa GR, Hulce JJ, Zanca C, et al. An LXR-cholesterol axis creates a metabolic co-dependency for brain cancers. *Cancer Cell*. 2016;30:683–693.
- Lin L, Desai R, Wang X, Lo EH, Xing C. Characteristics of primary rat microglia isolated from mixed cultures using two different methods. *J Neuroinflammation*. 2017;14:101.
- Schreiner B, Romanelli E, Liberski P, et al. Astrocyte depletion impairs redox homeostasis and triggers neuronal loss in the adult CNS. *Cell Rep*. 2015;12:1377–1384.
- Ma X, Bi E, Lu Y, et al. Cholesterol induces CD8+ T cell exhaustion in the tumor microenvironment. *Cell Metab*. 2019;30:143–156.e5.
- Walter DM, Venancio OS, Buza EL, et al. Systematic *in vivo* inactivation of chromatin-regulating enzymes identifies Setd2 as a potent tumor suppressor in lung adenocarcinoma. *Cancer Res*. 2017;77:1719–1729.
- Zur H, Ruppin E, Shlomi T. iMAT: An integrative metabolic analysis tool. *Bioinformatics*. 2010;26:3140–3142.
- Bordbar A, Monk JM, King ZA, Palsson BO. Constraint-based models predict metabolic and associated cellular functions. *Nat Rev Genet*. 2014;15:107–120.
- Ulitsky I, Maron-Katz A, Shavit S, et al. Expander: From expression microarrays to networks and functions. *Nat Protoc*. 2010;5:303–322.

34. Raudvere U, Kolberg L, Kuzmin I, et al. g:Profiler: A web server for functional enrichment analysis and conversions of gene lists (2019 update). *Nucleic Acids Res.* 2019;47(W1):W191–W198.
35. Sanz E, Yang L, Su T, Morris DR, McKnight GS, Amieux PS. Cell-type-specific isolation of ribosome-associated mRNA from complex tissues. *Proc Natl Acad Sci U S A.* 2009;106:13939–13944.
36. Bray NL, Pimentel H, Melsted P, Pachter L. Near-optimal probabilistic RNA-seq quantification. *Nat Biotechnol.* 2016;34:525–527.
37. Li B, Dewey CN. RSEM: accurate transcript quantification from RNA-Seq data with or without a reference genome. *BMC Bioinformatics.* 2011;12:323.
38. Anders S, Huber W. Differential expression analysis for sequence count data. *Genome Biol.* 2010;11:R106.
39. Kolde R, Vilo J. GOSummary: an R Package for visual functional annotation of experimental data. *F1000Research* 2015;4:574.
40. Tang Z, Li C, Kang B, Gao G, Li C, Zhang Z. GEPIA: A web server for cancer and normal gene expression profiling and interactive analyses. *Nucleic Acids Res.* 2017;45:W98–W102.
41. Zhao Z, Zhang KN, Wang Q, et al. Chinese Glioma Genome Atlas (CGGA): A comprehensive resource with functional genomic data from Chinese glioma patients. *Genom Proteom Bioinf.* 2021; 19:1–12.
42. Darmanis S, Sloan SA, Croote D, et al. Single-cell RNA-seq analysis of infiltrating neoplastic cells at the migrating front of human glioblastoma. *Cell Rep.* 2017;21:1399–1410.
43. Le T, Phan T, Pham M, et al. BBrowser: Making single-cell data easily accessible. *bioRxiv.* [Preprint] <https://doi.org/10.1101/2020.12.11.414136>
44. Wu YE, Pan L, Zuo Y, Li X, Hong W. Detecting activated cell populations using single-cell RNA-seq. *Neuron.* 2017;96:313–329.e6.
45. Zhong S, Zhang S, Fan X, et al. A single-cell RNA-seq survey of the developmental landscape of the human prefrontal cortex. *Nature.* 2018;555:524–528.
46. Doron H, Amer M, Ershaid N, et al. Inflammatory activation of astrocytes facilitates melanoma brain tropism via the CXCL10-CXCR3 signaling axis. *Cell Rep.* 2019;28:1785–1798.e6.
47. Liu Y, Yuelling LW, Wang Y, et al. Astrocytes promote medulloblastoma progression through hedgehog secretion. *Cancer Res.* 2017;77:6692–6703.
48. Anderson MA, Burda JE, Ren Y, et al. Astrocyte scar formation aids central nervous system axon regeneration. *Nature.* 2016; 532:195–200.
49. Bush TG, Puvanachandra N, Horner CH, et al. Leukocyte infiltration, neuronal degeneration, and neurite outgrowth after ablation of scar-forming, reactive astrocytes in adult transgenic mice. *Neuron.* 1999;23:297–308.
50. Wang JL, Scheitler KM, Wenger NM, Elder JB. Viral therapies for glioblastoma and high-grade gliomas in adults: A systematic review. *Neurosurg Focus.* 2021;50:E2.
51. Liddelow SA, Guttenplan KA, Clarke LE, et al. Neurotoxic reactive astrocytes are induced by activated microglia. *Nature.* 2017; 541:481–487.
52. Flores-Toro JA, Luo D, Gopinath A, et al. CCR2 inhibition reduces tumor myeloid cells and unmasks a checkpoint inhibitor effect to slow progression of resistant murine gliomas. *Proc Natl Acad Sci U S A.* 2020;117:1129–1138.
53. Piperi C, Papavassiliou KA, Papavassiliou AG. Pivotal role of STAT3 in shaping glioblastoma immune microenvironment. *Cells.* 2019;8:1398.
54. Akkari L, Bowman RL, Tessier J, et al. Dynamic changes in glioma macrophage populations after radiotherapy reveal CSF-1R inhibition as a strategy to overcome resistance. *Sci Transl Med.* 2020;12:eaaw7843.
55. Neal ML, Boyle AM, Budge KM, Safadi FF, Richardson JR. The glycoprotein GPNMB attenuates astrocyte inflammatory responses through the CD44 receptor. *J Neuroinflammation.* 2018; 15:73.
56. Kuan CT, Wakiya K, Keir ST, et al. Affinity-matured anti-glycoprotein NMB recombinant immunotoxins targeting malignant gliomas and melanomas. *Int J Cancer.* 2011;129:111–121.
57. Hambardzumyan D, Gutmann DH, Kettenmann H. The role of microglia and macrophages in glioma maintenance and progression. *Nat Neurosci.* 2016;19:20–27.
58. Klemm F, Maas RR, Bowman RL, et al. Interrogation of the micro-environmental landscape in brain tumors reveals disease-specific alterations of immune cells. *Cell.* 2020;181:1643–1660.e17.
59. Lepore F, D'Alessandro G, Antonangeli F, et al. CXCL16/CXCR6 axis drives microglia/macrophages phenotype in physiological conditions and plays a crucial role in glioma. *Front Immunol.* 2018;9:2750.
60. Izikson L, Klein RS, Charo IF, Weiner HL, Luster AD. Resistance to experimental autoimmune encephalomyelitis in mice lacking the CC chemokine receptor (CCR2). *J Exp Med.* 2000;192: 1075–1080.
61. Qian BZ, Pollard JW. Macrophage diversity enhances tumor progression and metastasis. *Cell.* 2010;141:39–51.
62. Colegio OR, Chu NQ, Szabo AL, et al. Functional polarization of tumour-associated macrophages by tumour-derived lactic acid. *Nature.* 2014;513:559–563.
63. Franklin RA, Liao W, Sarkar A, et al. The cellular and molecular origin of tumor-associated macrophages. *Science.* 2014;344:921–925.
64. Noy R, Pollard JW. Tumor-associated macrophages: From mechanisms to therapy. *Immunity.* 2014;41:49–61.
65. Hutter G, Theruvath J, Graef CM, et al. Microglia are effector cells of CD47-SIRP $\alpha$  antiphagocytic axis disruption against glioblastoma. *Proc Natl Acad Sci U S A.* 2019;116:997–1006.
66. Gabrilovich DI, Ostrand-Rosenberg S, Bronte V. Coordinated regulation of myeloid cells by tumours. *Nat Rev Immunol.* 2012; 12:253–268.
67. Abels ER, Maas SLN, Nieland L, et al. Glioblastoma-associated microglia reprogramming is mediated by functional transfer of extracellular miR-21. *Cell Rep.* 2019;28:3105–3119.e7.
68. Saha D, Martuza RL, Rabkin SD. Macrophage polarization contributes to glioblastoma eradication by combination immunovirotherapy and immune checkpoint blockade. *Cancer Cell.* 2017;32:253–267.e5.
69. Rosenzweig N, Dvir-Szternfeld R, Tsitsou-Kampeli A, et al. PD-1/PD-L1 checkpoint blockade harnesses monocyte-derived macrophages to combat cognitive impairment in a tauopathy mouse model. *Nat Commun.* 2019;10:465.
70. Hwang SY, Yoo BC, Jung JW, et al. Induction of glioma apoptosis by microglia-secreted molecules: The role of nitric oxide and cathepsin B. *Biochim Biophys Acta.* 2009;1793: 1656–1668.
71. Xue N, Zhou Q, Ji M, et al. Chlorogenic acid inhibits glioblastoma growth through repolarizing macrophage from M2 to M1 phenotype. *Sci Rep.* 2017;7:39011.
72. Casas AI, Hassan AA, Larsen SJ, et al. From single drug targets to synergistic network pharmacology in ischemic stroke. *Proc Natl Acad Sci U S A.* 2019;116:7129–7136.
73. Mayo L, Stein R. Characterization of LPS and interferon- $\gamma$  triggered activation-induced cell death in N9 and primary microglial cells: Induction of the mitochondrial gateway by nitric oxide. *Cell Death Differ.* 2007;14:183–186.

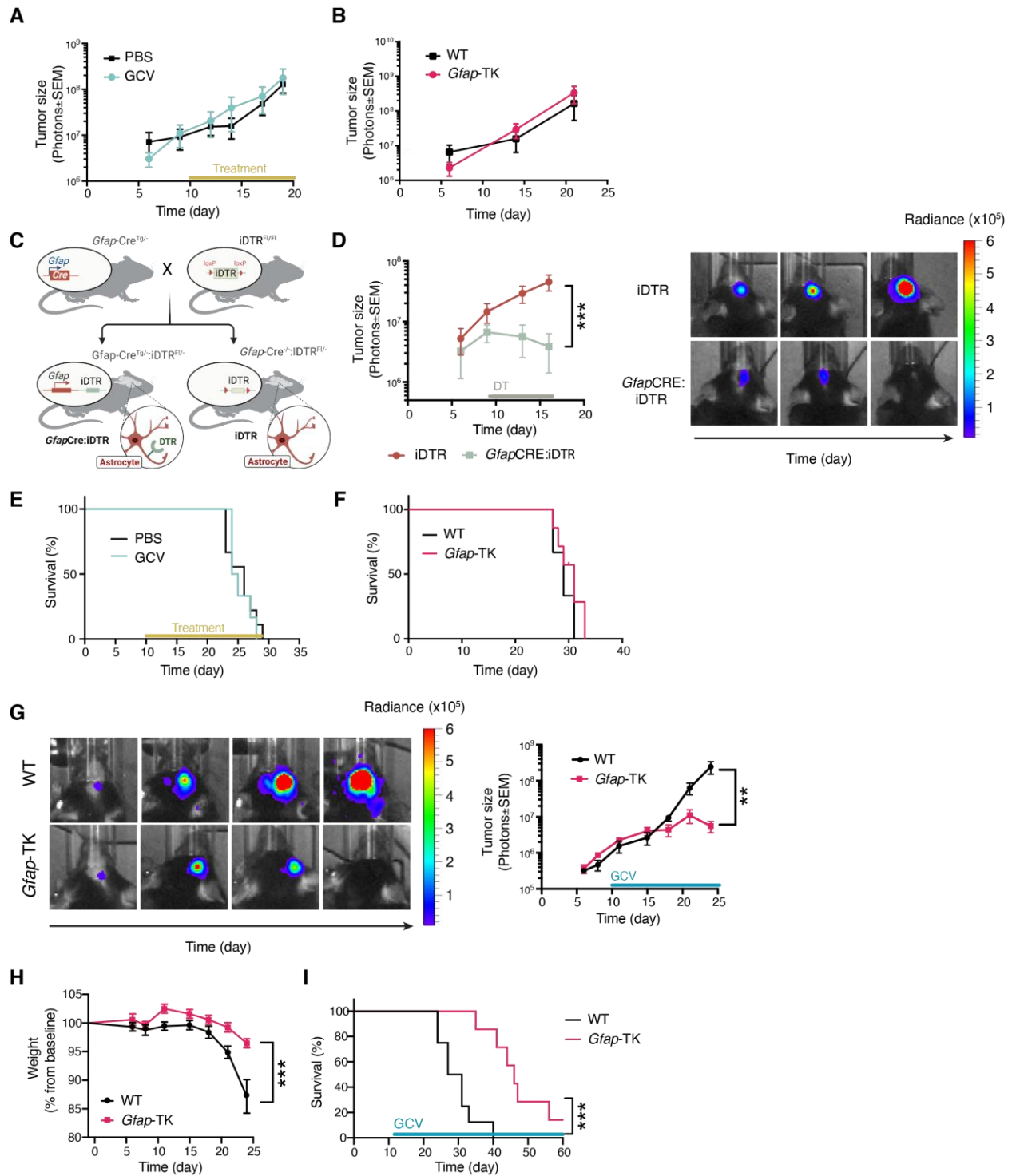
74. Vander Heiden MG, DeBerardinis RJ. Understanding the intersections between metabolism and cancer biology. *Cell*. 2017;168:657–669.
75. Styr B, Gonen N, Zarhin D, et al. Mitochondrial regulation of the hippocampal firing rate set point and seizure susceptibility. *Neuron*. 2019;102:1009–1024.e8.
76. Lewis NE, Schramm G, Bordbar A, et al. Large-scale in silico modeling of metabolic interactions between cell types in the human brain. *Nat Biotechnol*. 2010;28:1279–1285.
77. Maxfield FR, Tabas I. Role of cholesterol and lipid organization in disease. *Nature*. 2005;438:612–621.
78. Dang EV, McDonald JG, Russell DW, Cyster JG. Oxysterol restraint of cholesterol synthesis prevents AIM2 inflammasome activation. *Cell*. 2017;171:1057–1071.e11.
79. Smith B, Land H. Anticancer activity of the cholesterol exporter ABCA1 gene. *Cell Rep*. 2012;2:580–590.
80. Kuzu OF, Noory MA, Robertson GP. The role of cholesterol in cancer. *Cancer Res*. 2016;76:2063–2070.
81. Phillips RE, Yang Y, Smith RC, et al. Target identification reveals lanosterol synthase as a vulnerability in glioma. *Proc Natl Acad Sci U S A*. 2019;116:7957–7962.
82. Itoh N, Itoh Y, Tassoni A, et al. Cell-specific and region-specific transcriptomics in the multiple sclerosis model: Focus on astrocytes. *Proc Natl Acad Sci U S A*. 2018;115:E302–E309.
83. Montero J, Morales A, Llacuna L, et al. Mitochondrial cholesterol contributes to chemotherapy resistance in hepatocellular carcinoma. *Cancer Res*. 2008;68:5246–5256.
84. Courtney R, Landreth GE. LXR regulation of brain cholesterol: From development to disease. *Trends Endocrinol Metab*. 2016;27:404–414.
85. Haimon Z, Volaski A, Orthgiess J, et al. Re-evaluating microglia expression profiles using RiboTag and cell isolation strategies. *Nat Immunol*. 2018;19:636–644.
86. Boisvert MM, Erikson GA, Shokhirev MN, Allen NJ. The aging astrocyte transcriptome from multiple regions of the mouse brain. *Cell Rep*. 2018;22:269–285.
87. Friebel E, Kapolou K, Unger S, et al. Single-cell mapping of human brain cancer reveals tumor-specific instruction of tissue-invading leukocytes. *Cell*. 2020;181:1626–1642.e20.
88. Chen Z, Feng X, Herting CJ, et al. Cellular and molecular identity of tumor-associated macrophages in glioblastoma. *Cancer Res*. 2017;77:2266–2278.
89. Markovic DS, Vinnakota K, van Rooijen N, et al. Minocycline reduces glioma expansion and invasion by attenuating microglial MT1-MMP expression. *Brain Behav Immun*. 2011;25:624–628.
90. Bunse L, Pusch S, Bunse T, et al. Suppression of antitumor T cell immunity by the oncometabolite (R)-2-hydroxyglutarate. *Nat Med*. 2018;24:1192–1203.
91. Tilghman J, Wu H, Sang Y, et al. HMMR maintains the stemness and tumorigenicity of glioblastoma stem-like cells. *Cancer Res*. 2014;74:3168–3179.
92. Li D, Zhang J, Liu Q. Brain cell type-specific cholesterol metabolism and implications for learning and memory. *Trends Neurosci*. 2022;45:401–414.
93. Escartin C, Galea E, Lakatos A, et al. Reactive astrocyte nomenclature, definitions, and future directions. *Nat Neurosci*. 2021;24:312–325.
94. Anderson MA, Ao Y, Sofroniew MV. Heterogeneity of reactive astrocytes. *Neurosci Lett*. 2014;565:23–29.
95. Batiuk MY, Martirosyan A, Wahis J, et al. Identification of region-specific astrocyte subtypes at single cell resolution. *Nat Commun*. 2020;11:1220.
96. Wheeler MA, Clark IC, Tjon EC, et al. MAFG-driven astrocytes promote CNS inflammation. *Nature*. 2020;578:593–599.
97. Habib N, McCabe C, Medina S, et al. Disease-associated astrocytes in Alzheimer's disease and aging. *Nat Neurosci*. 2020;23:701–706.
98. Kambach DM, Halim AS, Cauer AG, et al. Disabled cell density sensing leads to dysregulated cholesterol synthesis in glioblastoma. *Oncotarget*. 2017;8:14860–14875.
99. Moffett J, Kratz E, Florkiewicz R, Stachowiak MK. Promoter regions involved in density-dependent regulation of basic fibroblast growth factor gene expression in human astrocytic cells. *Proc Natl Acad Sci U S A*. 1996;93:2470–2475.

# **Astrocyte immunometabolic regulation of the tumor microenvironment drives glioblastoma pathogenicity**

Rita Perelroizen<sup>1,†</sup>, Bar Philosof<sup>1,†</sup>, Noga Budick-Harmelin<sup>2</sup>, Tom Chernobylsky<sup>2</sup>, Ariel Ron<sup>1</sup>,  
Katzir Rotem<sup>3</sup>, Dor Shimon<sup>2</sup>, Adi Tessler<sup>2</sup>, Orit Adir<sup>2</sup>, Anat Gaoni-Yogev<sup>2</sup>, Tom Meyer<sup>1</sup>, Avivit  
Krivitsky<sup>2</sup>, Nuphar Shidlovsky<sup>2</sup>, Asaf Madi<sup>4</sup>, Ruppin Eytan<sup>3</sup> and Lior Mayo<sup>1,2\*</sup>

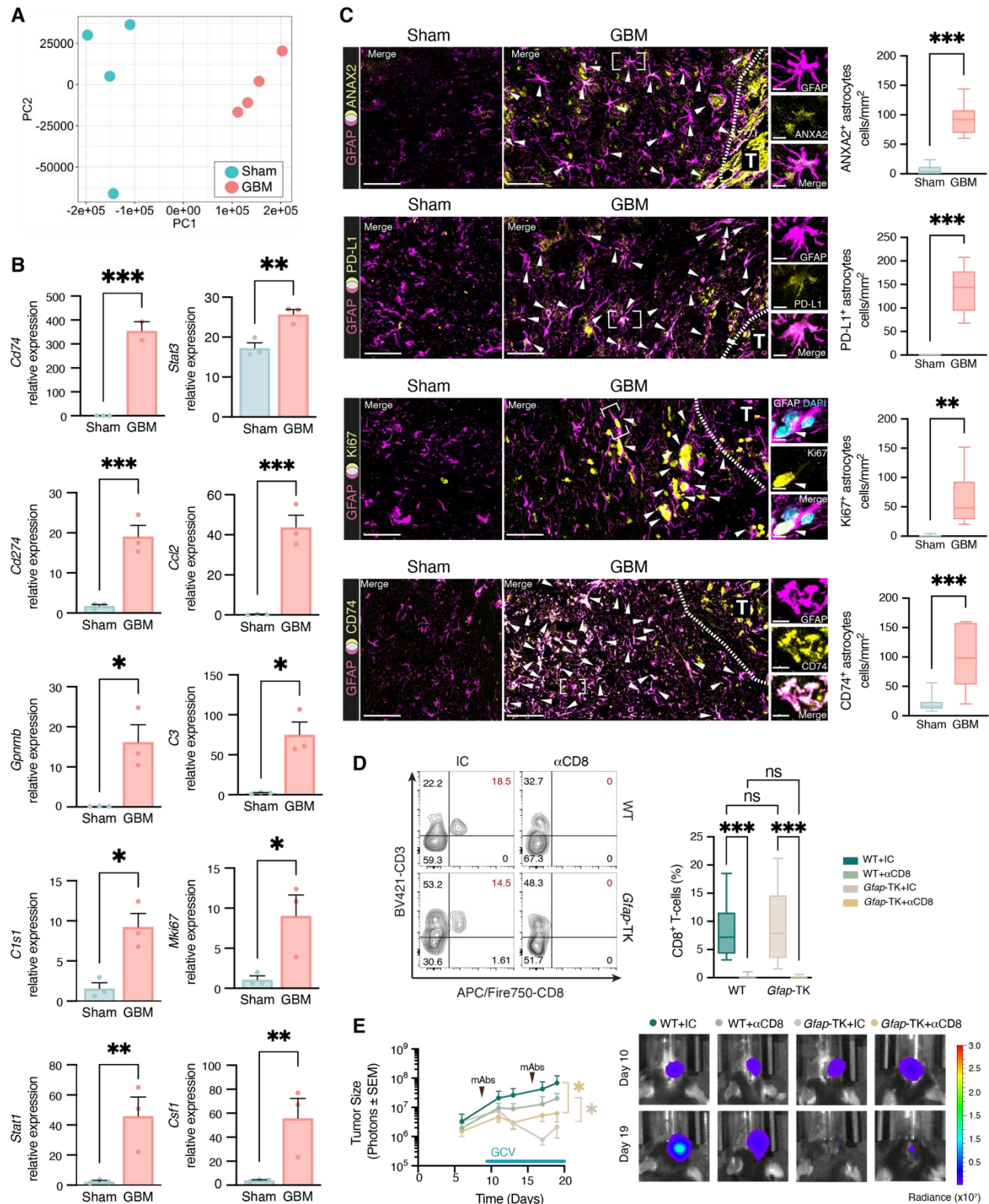
## **Supplementary material:**

1. Supplementary Figures 1-8
2. Supplementary Tables 1-3



**Supplementary Figure 1. Tumor-associated astrocyte depletion halts glioblastoma progression.** (A-B) Tumor size of GL261-bearing mice as determined by bioluminescence imaging. A, GL261 cells were intracranially implanted into WT mice. GBM-bearing mice were treated daily with Ganciclovir (GCV, 25mg/kg) or vehicle (PBS) from day 10 until the

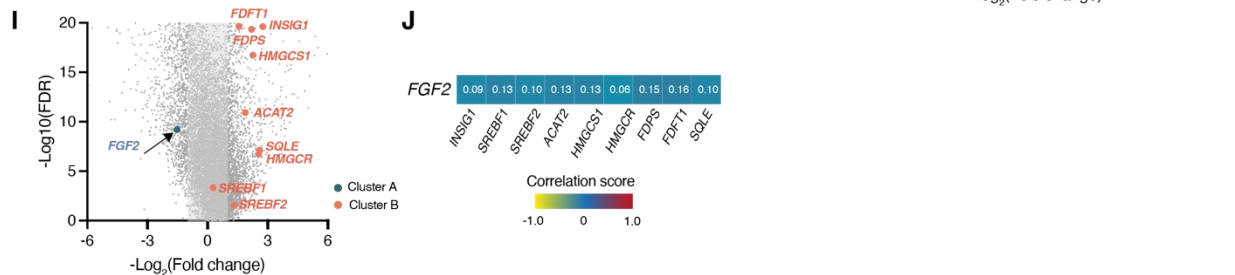
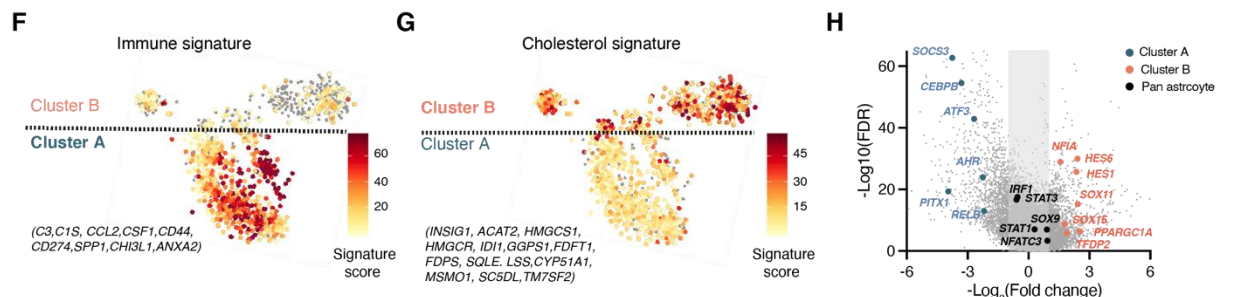
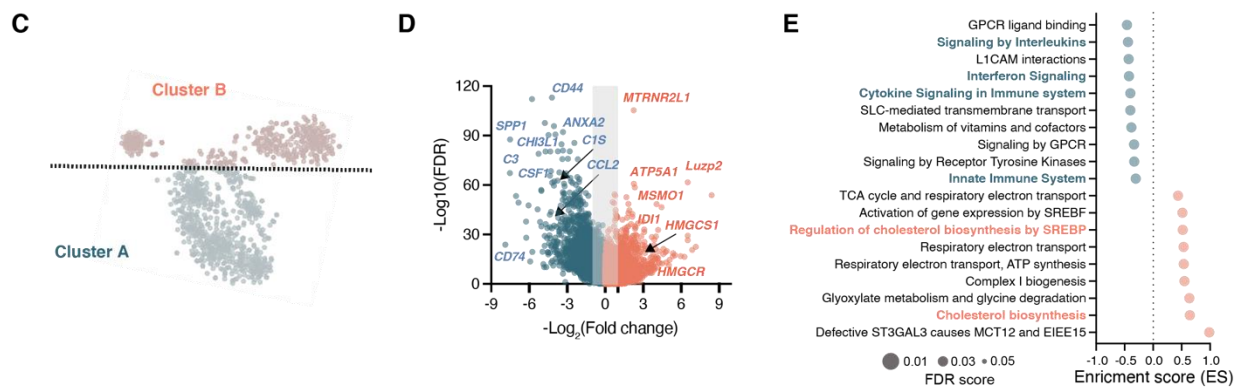
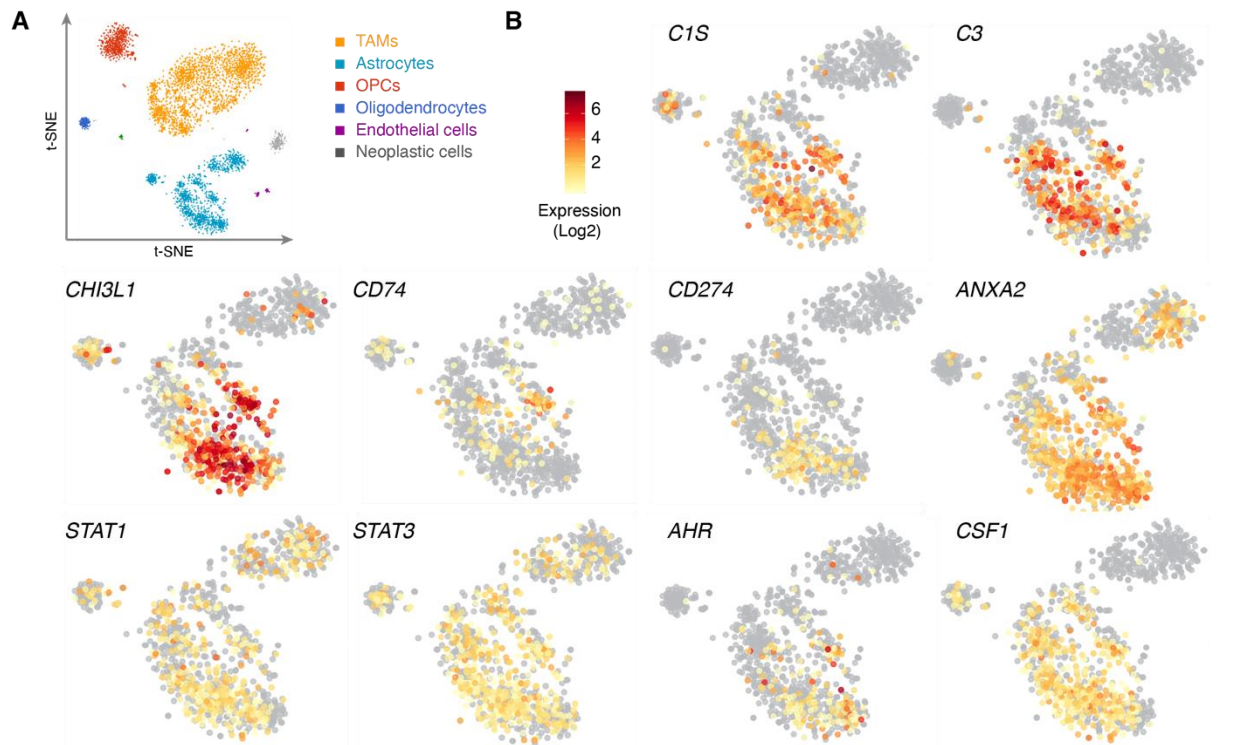
experimental end. Data are representative of two independent experiments with  $n = 8$  mice/group. **(B)** GL261 cells were intracranially implanted into WT or *Gfap*-TK mice. Data are representative of two independent experiments with  $n = 7$  mice/group. **(C)** *Gfap*CRE:iDTR breeding scheme. Mice in which the expression of the DT receptor (DTR) from a ubiquitously active promoter is prevented by a loxP-flanked stop cassette (iDTR)<sup>1</sup> were crossed with transgenic mice expressing the Cre recombinase under the control of the GFAP promoter to generate *Gfap*CRE:iDTR mice, in which DTR expression is limited to GFAP<sup>+</sup> astrocytes, resulting in their depletion following DT-A administration<sup>2</sup>. **(D)** iDTR or *Gfap*CRE:iDTR littermates, were intracranially implanted with GL261. Ten days later mice were treated daily with DT-A (1100ng/mice nasally). Tumor size was analyzed by bioluminescence imaging. Data are representative of two independent experiments with  $n = 7$  mice/group. **(E-F)** Kaplan-Meier curves assess the overall survival of mice from **A** and **B**, respectively. **(G-I)** Astrocyte ablation halts CT-2A glioma pathogenicity. CT-2A glioma cells were intracranially implanted into WT or *Gfap*-TK littermates and treated with GCV as in **(Fig 1D)**. Tumor growth was analyzed by bioluminescence imaging **(G)**, and mice weight loss and survival were monitored **(H and I, respectively)**. Data in **A,B,D,G, and H** are shown as mean  $\pm$  s.e.m. *P* values were determined by two-way ANOVA (**A,B,D,G, and H**) or Log rank (Mantel-Cox) test (**E,F and I**). \*\**P*<0.01, \*\*\**P*<0.001.



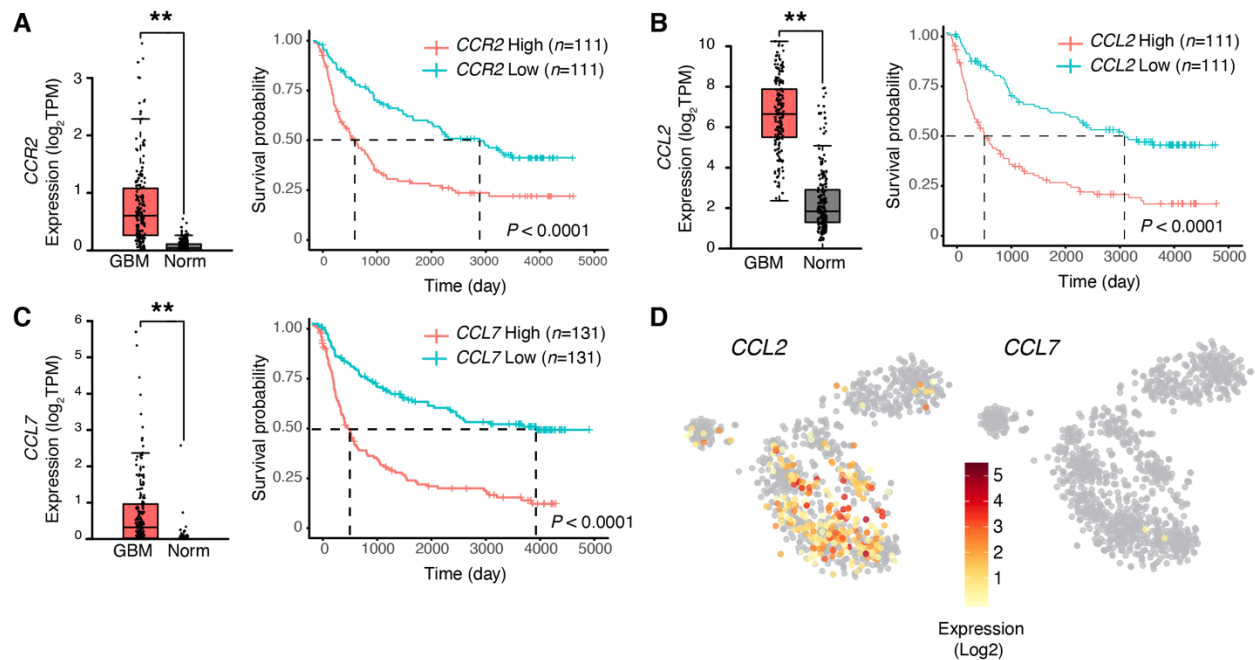
**Supplementary Figure 2. Transcriptomic analysis of tumor-associated astrocytes.** (A) PCA of differentially regulated genes of RiboTag-isolated astrocytes (as in Fig 2) from PBS-injected mice (Sham, pink) or GL261 GBM-bearing mice (GBM, blue). PC1 was associated with the



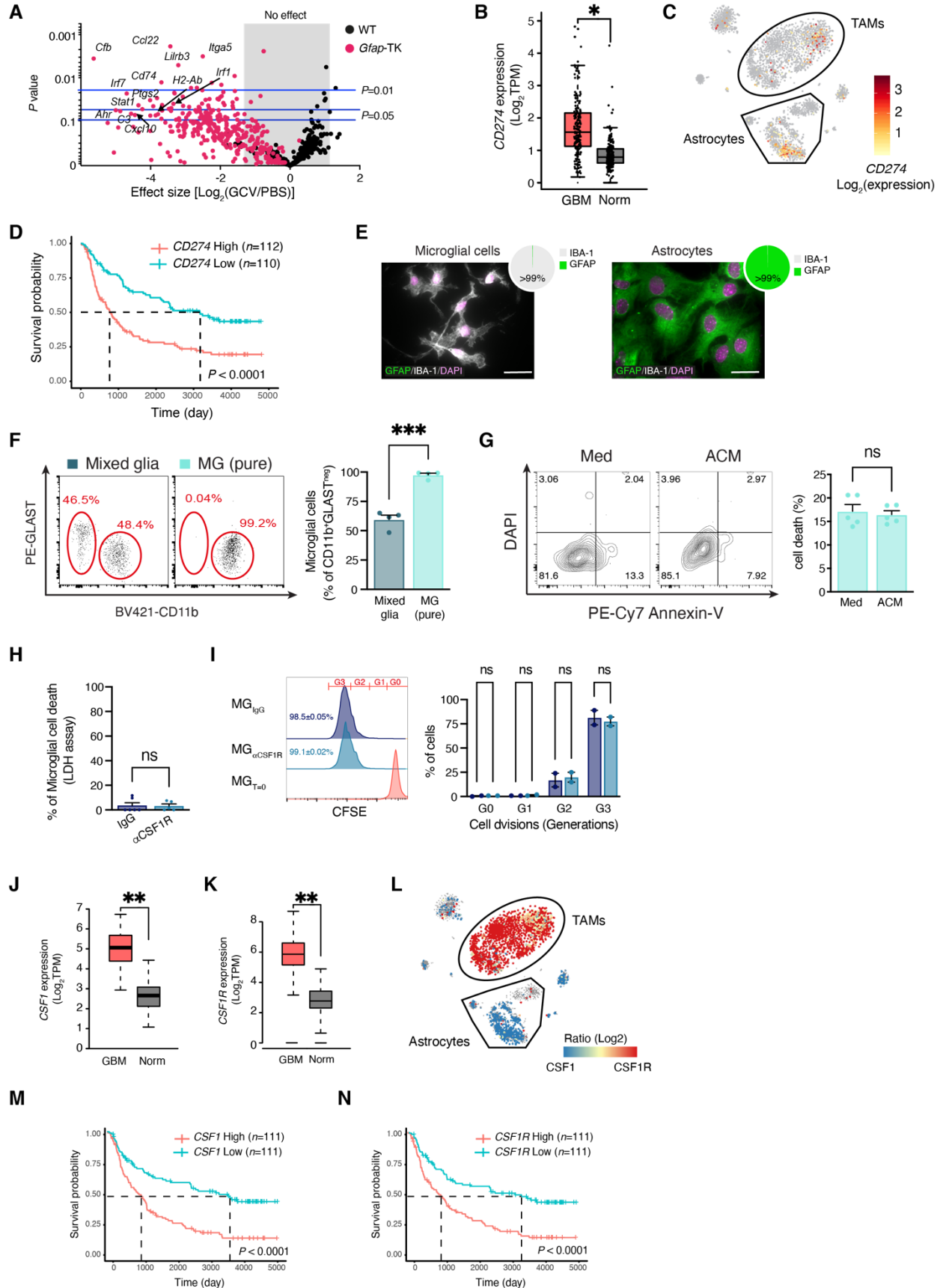
variance within the *sham* and *GBM* data sets, whereas PC2 was associated with the variance between each group. **(B)** Validation of RNA seq data in different biological samples. qPCR analysis of *Cd274*, *Ccl2*, *Stat1*, *Cd74*, *Stat3*, *Csf1*, *Gpnmb*, *C3*, *C1s1*, and *Mki67* expression in RiboTag-isolated astrocytes from sham-injected or GBM-implanted injected mice; expression normalized to *Ppia*. Data are representative of 3 independent experiments ( $n = 3$  biologically independent samples). Data are shown as mean  $\pm$  s.e.m. **(C)** Immunohistochemistry analysis of GFAP (magenta) co-localization with Annexin A2 (ANXA2, yellow), PD-L1 (yellow), Ki67 (yellow), or CD74 (yellow) of sham-injected or GBM-bearing mice. Representative images on the left, box-plot analysis of the antigen-positive astrocytes per  $\text{cm}^2$  ( $n = 9$ ), on the right. Scale bars, 500  $\mu\text{m}$  (left), 5  $\mu\text{m}$  (right). Co-localization (white) is identified by white arrowheads. Data are shown as median, interquartile interval, minimum, and maximum values. **(D,E)** CD8<sup>+</sup> T-cell depletion in WT or *Gfap*-TK mice GBM-bearing mice. GL261 cells were intracranially implanted, and the mice were treated daily with GCV from day 9 until the experimental end (as in Fig 1D), and intraperitoneally injected (black arrows) with CD8 depleting mAbs ( $\alpha\text{CD8}$ ) or isotype control (IC) (0.1 mg/mouse, as in<sup>3</sup>). Representative data of two independent experiments ( $n = 9$  mice/group). **(D)** Analysis of the CD8<sup>+</sup> T-cells frequency in the blood. Representative flow cytometry plots of CD3<sup>+</sup>/CD8<sup>+</sup> staining are shown on the left and quantification analyses of CD8<sup>+</sup> T-cells frequency are on the right. **(E)** Tumor size of GL261-bearing mice as determined by bioluminescence imaging. *P* values were determined by two-sided Student's t-tests **(B,C)** or two-way ANOVA **(D,E)**. \* $P < 0.05$ , \*\* $P < 0.01$ , \*\*\* $P < 0.001$ .



**Supplementary Figure 3. Transcriptomic analysis of human tumor-associated astrocytes (A, B)** Analysis of single-cell data of the tumor microenvironment of IDH1<sup>neg</sup> grade IV GBM patients performed on data by Darmanis et. al<sup>4</sup>. **(A)** unbiased clustering of the TAMs (1842 cells, orange), TAAs (1052 cells, light blue), oligodendrocyte precursor cells (OPCs, 406 cells, red), oligodendrocytes (81 cells, dark blue), and endothelial cells (50 cells, purple), neurons (21, green) and neoplastic cells (137, gray) defined based on the expression of known markers<sup>5-7</sup>), presented as color-coded TSNE plot. **(B)** Heat map overly of the scRNAseq gene expression intensity within the astrocyte cluster of *C1S*, *C3*, *CHI3L1*, *CD74*, *CD274*, *ANXA2*, *STAT1*, *STAT3*, *AHR*, and *CSF1*. Expression levels are defined by color-coded expression as indicated (from yellow to red; gray coloring indicates that the transcript was not detected). **(C-H)** Analysis of astrocyte diversity. **(C,D)** Sub clustering of astrocytes based on differential expression. **(C)** Color-coded TSNE plot of cluster A (Blue, 599 cells) and cluster B (Pink, 453 cells). **(D)** Volcano plot of gene expression in astrocytes, color-coded by the cluster enrichment. **(E)** Top 20 Functional enrichment pathways (FDR<0.05) in the astrocyte clusters, color-coded by the cluster enrichment. **(F,G)** Heat map overly of the scRNAseq gene expression intensity of astrocyte immune and cholesterol signatures **(F and G, respectively)**. Expression levels in heatmaps are color-coded (from yellow to red; Grey indicates that the transcript was not detected). Genes associated with each signature are stated at the bottom of the corresponding heat map. Signature score is defined as the sum of all relevant transcripts per cell. **(H)** Expression levels overlay of significant (FDR<0.001) transcription factors on volcano plot from **(D)**, color-coded by association with cluster A (blue), B (pink), or expressed evenly between the two clusters (pan-astrocyte expression, black). **(I,J)** Analysis of *FGF2* expression and its correlation to cholesterol synthesis genes (*INSG1*, *SREBF1*, *SREBF2*, *ACAT2*, *HMGCS1*, *HMGCR*, *FDPS*, *FDFT1*, and *SQLE*), which are regulated by astrocyte cell density<sup>8</sup>. **(I)** Heat map overly of the transcripts expression levels in the astrocytes, color-coded by their cluster association (as in **H**). **(J)** Heat map of the Jaccard correlation index between *FGF2* transcript to the cholesterol synthesis genes. Correlation score is noted within each cell. Correlation is color-coded [negative (yellow) , natural (blue) and purple (positive)].

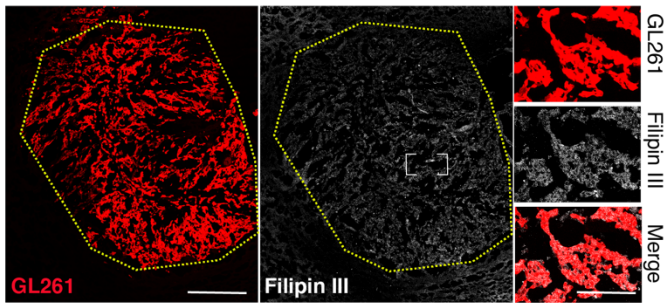
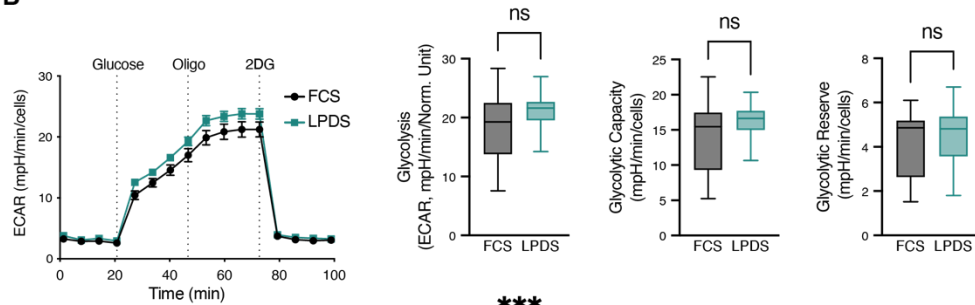
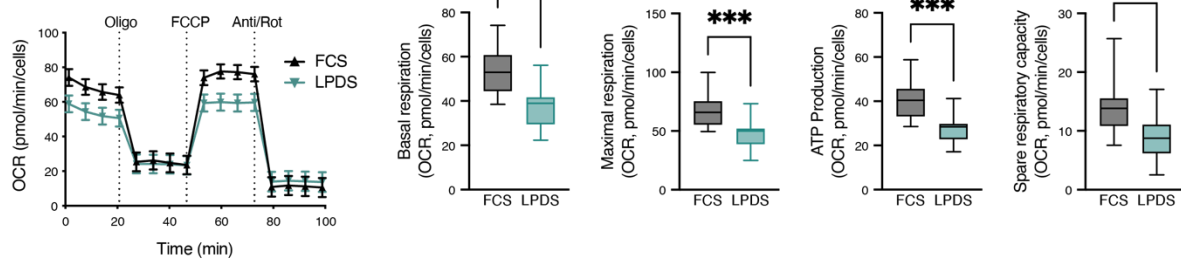
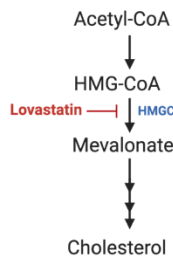
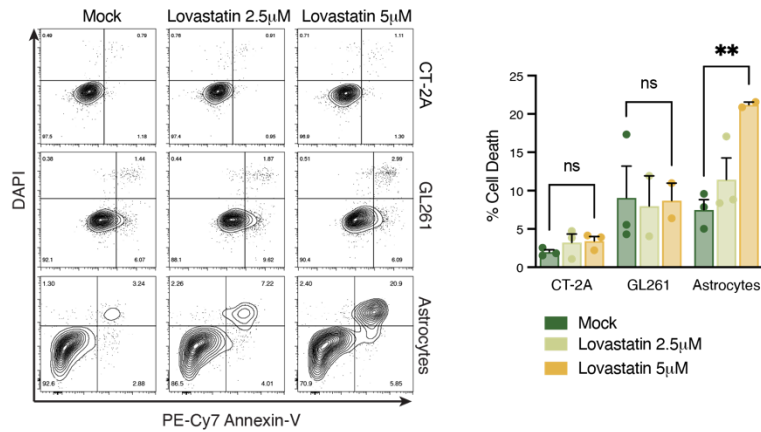
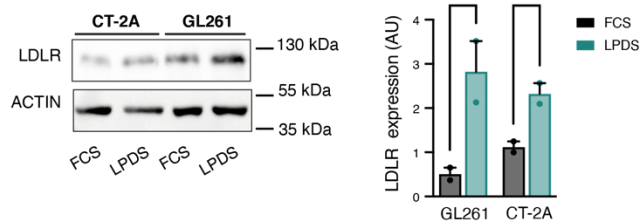
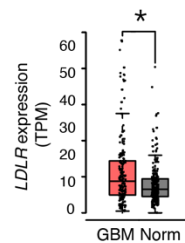


**Supplementary Figure 4. Analysis of CCR2 pathway in human GBM.** (A-C) Analysis of gene expression (Box plots, left panel; n=163 GBM patients and 207 normal controls) and survival correlations (Kaplan-Meier Curve, right panel; n as indicated) for *CCR2* (A), *CCL2* (B) and *CCL7* (C). *n* represents the number of patients per group. Data are shown as mean ± s.e.m. *P* values were determined by or two-sided Student's (*t*-test, \**P*<0.01) or Log-rank (Mantel-Cox) tests (survival, *P*<0.0001). (D) Heat map overly of the scRNAseq gene expression intensity of *CCL2*, and *CCL7* in tumor-associated astrocyte cluster of GBM patients<sup>4</sup> (as in **Supplementary Fig 3B**). Expression levels are defined by color-coded expression (from yellow to red; Grey indicates that the transcript was not detected).



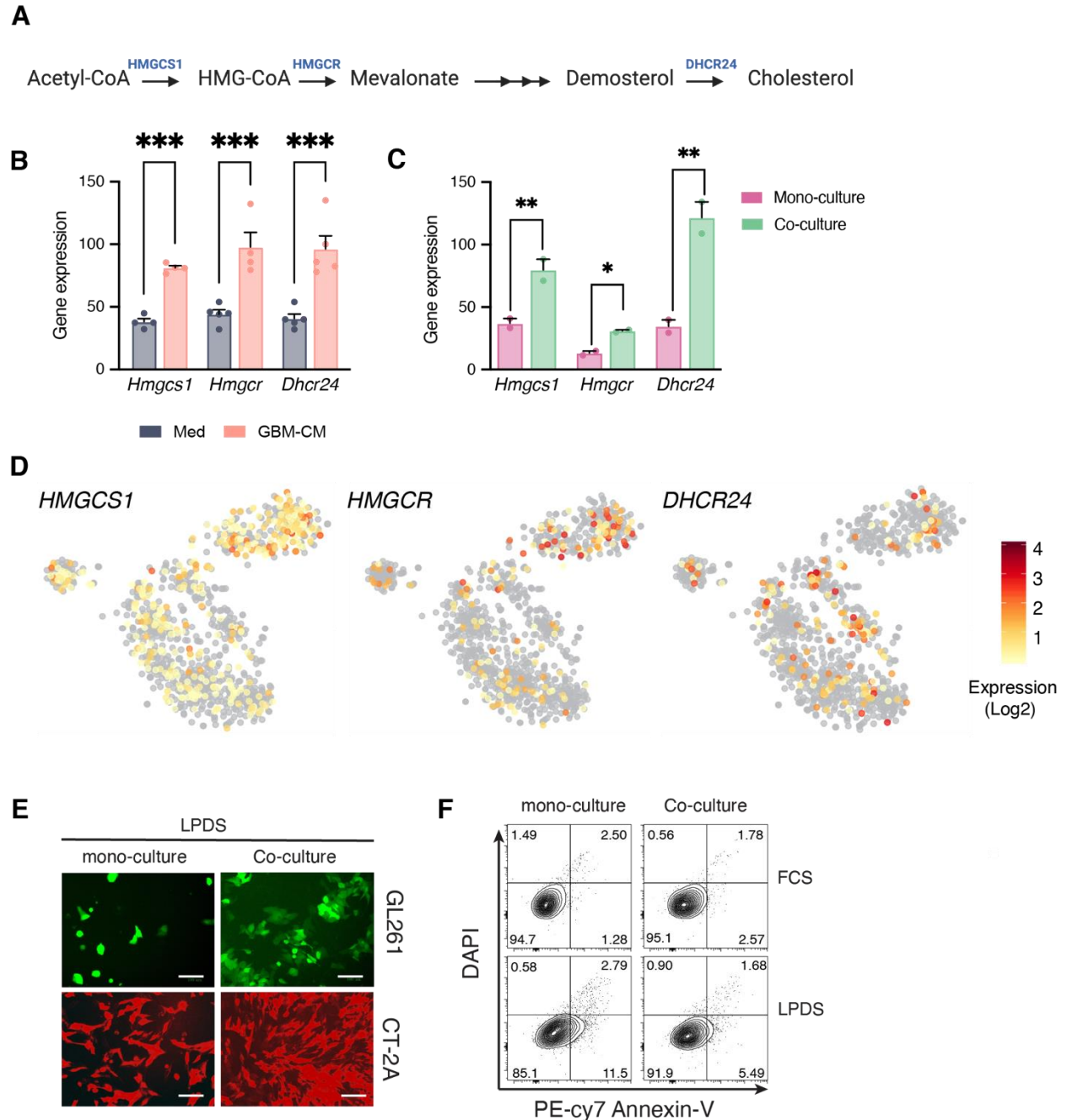
**Supplementary Figure 5. Profile of Tumor-associated Macrophages in Glioblastoma.** (A) Volcano plot of differential gene expression in FACS-sorted TAMs from GCV-treated WT (black) and *Gfap*-TK (pink) GL261-bearing mice. (B) Box plot analysis of TCGA data of CD274 gene expression in GBM ( $n=163$ ) and normal (Norm;  $n=207$ ) patients. (C) Heat map overlay of the scRNAseq gene expression intensity of *CD274* in GBM patients<sup>4</sup> (TAM and TAA clusters areas in **Supplementary Fig 3A**). Expression levels are defined by color-coded expression (from yellow to red; Grey indicates that the transcript was not detected). (D) Kaplan-Meier curves assessing overall survival of GBM patients based on CD274 expression; n represent the number of patients per group. (E) Representative fluorescent images of primary mouse microglial cells (left) and primary astrocytes, stained for GFAP (green), IBA-1 (white), and nuclei (DAPI, magenta). scale bars, 20  $\mu\text{m}$  (F) Mixed glial cultures were left untreated or subject to mild trypsinization<sup>9</sup>, isolating the microglial cells [MG (pure)]. Representative flow cytometry plots of CD11b/GLAST staining from each group are shown on the left and quantification analyses of CD11b<sup>+</sup> microglial cell frequencies are on the right ( $n = 4$  biologically independent experiments). Data are shown as mean  $\pm$  s.e.m.  $P$  values were determined by or two-sided Student's t-test (\*\*\*,  $P < 0.001$ ). (G) Pure microglial cultures were prepared, treated with astrocytes conditioned medium (ACM) or control medium (Med), and co-cultured with GFP<sup>+</sup>-GL261 cells for 48h (as in **Fig 4G**). Representative flow cytometry plots of GFP-gated GL261 cells from each group are shown on the left, and quantification analyses of cell death are on the right ( $n = 2$  biologically independent experiments). Data are shown as mean  $\pm$  s.e.m.  $P=0.678$  by two-sided Student's t-test. (H,I) pure microglial cultures were prepared, treated, and co-incubated with isotype control or CSF1R blocking mAbs (25 $\mu\text{g/ml}$ ) for 48h, as in (**Fig 4K**). Microglial cell death and proliferation were then analyzed by LDH assay (H) and CellTrace™ Violet staining (I). Representative flow cytometry plots are shown on the left and quantification analyses of the percentage of proliferating cells in each generation are on the right ( $n = 2$ ). Data are representative of two independent experiments. Data are shown as mean  $\pm$  s.e.m.  $P$  values were determined by two-sided Student's t-test;  $P = 0.89$  (H), or Two-way ANOVA, followed by Fisher's LSD post-hoc analysis;  $P > 0.99$  (I), ns, not significant. Box plot analysis of TCGA data of CSF1 (J) and CSF1R (K) gene expression in GBM ( $n=163$ ) and normal (Norm;  $n=207$ ) patients. (L) Heatmap overlay of CSF1/CSF1R ratio in the GBM TME, based on scRNAseq gene expression<sup>4</sup>. Ratio intensity is present by color; Blue – only CSF1 expressing cells, Yellow – the dual expression of CSF1 and CSF1R, and Red – cells that

only express CSF1R. (M,N) Kaplan-Meier curves assessing overall survival of GBM patient based on CSF1 and CSF1R expression; n represent the number of patients per group. Data are shown as mean  $\pm$  s.e.m. *P* values were determined by or two-sided Student's t-test (expression data, \**P*<0.01) or Log rank (Mantel-Cox) tests (survival, *P*<0.0001).

**A****B****C****D****E****F****G**

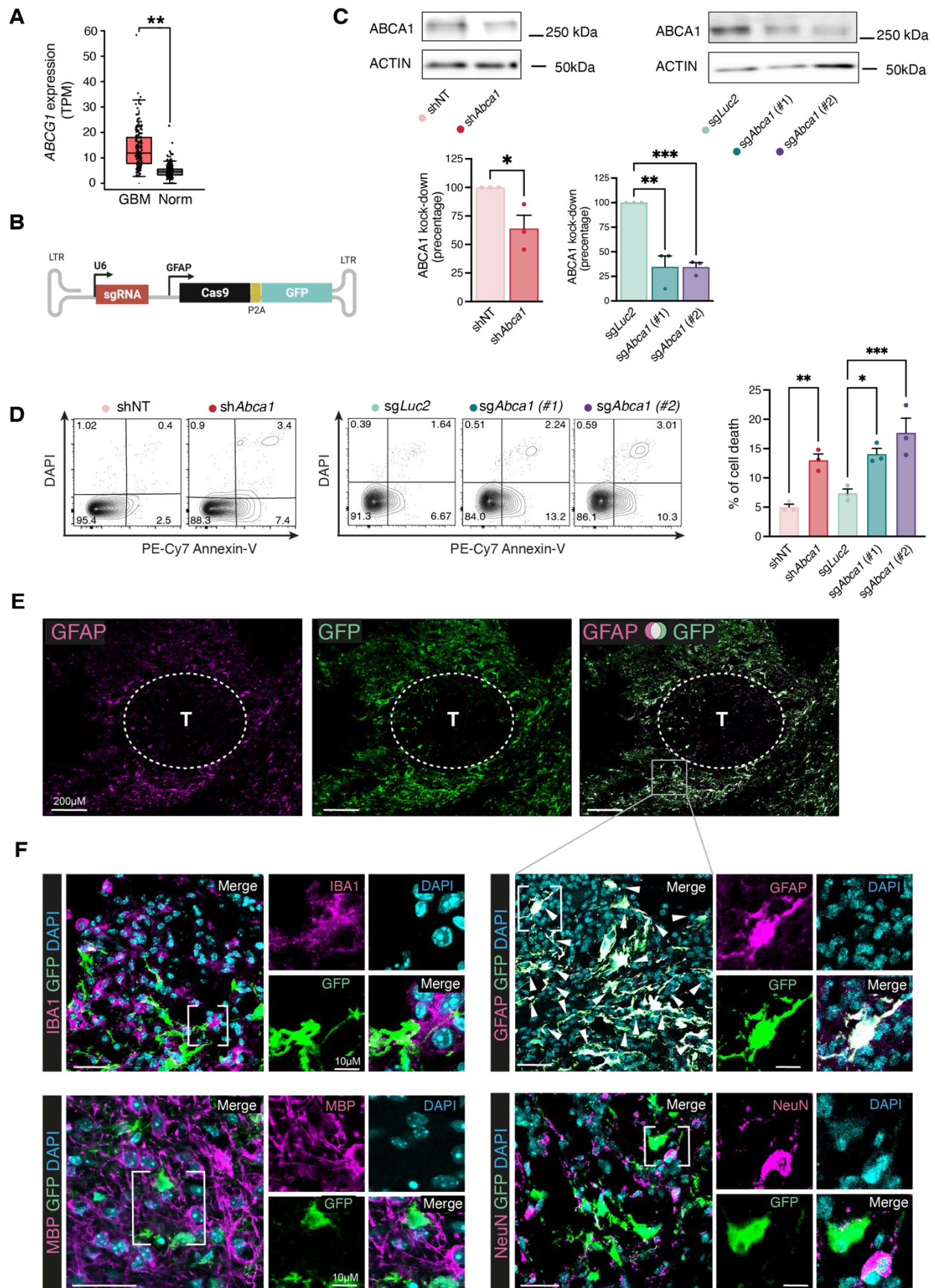


**Supplementary Figure 6. Astrocyte-derived cholesterol support glioma survival.** (A) Representative immunofluorescence images of cholesterol accumulation (Filipin III, white) in the GBM tumor (tdTomato+ GL261 cells, red), Tumor margins are indicated in yellow ( $n = 3$  biologically independent samples). Scale bars, 400  $\mu\text{m}$  (right), 150  $\mu\text{m}$  (left). (B,C) Real-time changes in the ECAR (B) and OCR (C) of CT-2A glioma cells, cultured in media supplemented with full serum (FCS) or lipoprotein-deprived serum (LPDS) for 18 h and measured using Seahorse. Oligo, oligomycin; FCCP, carbonyl cyanide4-(trifluoromethoxy) phenylhydrazine; R/A, rotenone plus antimycin A; 2-DG, 2-deoxy-d-glucose. Glycolysis, glycolytic capacity and glycolytic reserve are extracted from ECAR reading, and basal respiration, ATP production, Maximal respiration, and spare respiratory capacity were determined based on OCR. Data are representative of two independent experiments ( $n = 6$  technical replicates per experiment). (D) Scheme of cholesterol synthesis inhibition by HMGCR-inhibitor lovastatin. (E) Representative flow cytometry plots and quantification analyses of Annexin V/DAPI staining comparing astrocytes with CT-2A and GL261 cells after a 3-day treatment with the lovastatin. ( $n = 3$  biologically independent experiments). (F) Representative immunoblot and quantification analyses comparing LDLR protein levels in with CT-2A and GL261 cells cultured for 2 days in FCS or LPDS supplemented media. ( $n = 3$  biologically independent experiments). (G) Box plot analysis of TCGA gene expression for *LDLR* in normal ( $n=207$ ) or GBM patients ( $n=163$ ).  $n$  represents the number of patients per group. Data are shown as mean  $\pm$  s.e.m.  $P$  values were determined by two-sided Student's  $t$ -tests (B,C,F and G) or by one-way ANOVA, followed by Fisher's LSD post-hoc analysis (E). \* $P < 0.05$ , \*\* $P < 0.01$ , \*\*\* $P < 0.001$ .



**Supplementary Figure 7. Astrocyte-derived cholesterol support glioma survival.** (A) Scheme of *de-novo* cholesterol synthesis pathway. (B,C) qPCR analyses of *Hmgcs1*, *Hmgcr*, and *Dhcr24* expression in astrocytes treated with GBM-CM (B) or co-incubated for 24h with GL261 (C); expression normalized to *Ppia* ( $n = 4$  biologically independent experiments). (D) Heat map overly of the scRNAseq gene expression intensity of *HMGCS1*, *HMGCR*, and *DHC24* in tumor-associated astrocytes from GBM patients<sup>4</sup> (astrocyte cluster as in **Supplementary Fig 3A**). Expression levels are defined by color-coded expression (from yellow to red; Grey indicates that

the transcript was not detected). **(E,F)** Analysis of LPDS-induced glioma cell death, in the presence or absence of primary astrocytes, by Annexin-V assay. **(E)** Representative fluorescent images of murine GFP<sup>+</sup>-GL261 and tdTomato<sup>+</sup>-CT-2A glioma cells were co-cultured with or without primary mouse astrocytes ( $n = 4$  biologically independent experiments). **(F)** Representative flow cytometry plots and quantification analyses of Annexin V/DAPI staining comparing human U87EGFR $\nu$ III<sup>10</sup> glioma cells co-cultured with or human primary astrocytes for 5 days ( $n = 3$  biologically independent experiments). Data are shown as mean  $\pm$  s.e.m.  $P$  values were determined by a two-sided Student's t-test (**B** and **C**). \* $P < 0.05$ , \*\* $P < 0.01$ , \*\*\* $P < 0.001$ .



**Supplementary Figure 8. Astrocytic expression of ABCG1, ABCA1, and astrocyte-specific lentiviruses.** (A) Box plot analysis of TCGA gene expression for *ABCG1* in normal (Norm;  $n=207$ ) or GBM ( $n=163$ ) patients.  $n$  represents the number of patients per group (B-D) Primary astrocytes were transduced with RNAi encoding lentiviruses [Non-targeting shRNA (shNT) or *Abca1*-targeting shRNA (sh*Abca1*); Schematic map of the astrocyte-specific shRNA lentiviral vector in Fig. 6F], Or astrocyte-specific CRISPR-Cas9 lentivirus targeting the luciferase gene (sg*Luc2*; control), or *Abca1* sg*Abca1* (#1) and sg*Abca1* (#2); Schematic map of the astrocyte-specific CRISPR-Cas9-sgRNA lentiviral vector in (B). shRNA and sgRNA sequences are detailed in Supplementary Table 1. Transduced astrocytes were then co-cultured with CT-2A glioma cells in LPDS-media for 5 days, and LPDS-induced glioma cell death was determined by Annexin-V assay. (C) Representative immunoblot and quantification analyses comparing ABCA1 protein levels in transduced astrocytes ( $n = 3$  biologically independent experiments). (D) Representative flow cytometry plots of CT-2A glioma cells co-cultured for 5 days with transduced astrocytes are shown on the left and quantification analyses on the right ( $n = 3$  biologically independent experiments). Data are shown as mean  $\pm$  s.e.m.  $P$  values were determined by a two-sided Student's t-test (C) or by one-way ANOVA (C, D). \* $P < 0.05$ , \*\* $P < 0.01$ , \*\*\* $P < 0.001$ . (E,F) Expression of astrocyte-specific GFP-expressing *Gfap*-shRNA lentiviruses-injected GBM-bearing mice. (E) Representative immunofluorescence images of GFP (green) and GFAP (astrocytes, magenta), scale bars, 400  $\mu$ m (F) Representative immunofluorescence images of GFP expression (green) and cell makers for TAMs (IBA1, magenta), oligodendrocytes (MBP, magenta), astrocytes (GFAP, magenta), or neurons (NeuN, magenta). Colocalization (white) is identified by white arrowheads. Large scale image on the left, insert (white box) on the right. scale bars, 40  $\mu$ m, scale bar for insert 10  $\mu$ m. Data are representative of two independent experiments with  $n = 3$  mice/group.

**Supplementary Table I. Sequences used for generating ABCA1 RNAi vectors**

<b>ID</b>	<b>Name</b>	<b>Sequence (5'-&gt;3')</b>
1	shNT <sup>11</sup>	GAGTGCCACTTTCCGAATAAA
2	shAbca1	GCGCGATAGCGCTAATAATTT
3	gfaABC1D	GATCTAACATATCCTGGTGTGGAGTAGGGGACGCTGCTCTGACAGAGGCTCGGGGGCCTGA GCTGGCTCTGTGAGCTGGGGAGGAGGCAGACAGCCAGGCCTTGTCTGCAAGCAGACCTGGC AGCATTGGGCTGGCCGCCCCCAGGGCCTCCTTTCATGCCAGTGAATGACTCACCTTGGC ACAGACACAATGTTTCGGGGTGGGCACAGTGCCTGCTTCCC GCCGACCCCCAGCCCCCTCA AATGCCTTCCGAGAAGCCATTGAGCAGGGGGCTTGCATTGCACCCAGCCTGACAGCCTG GCATCTTGGGATAAAAGCAGCACAGCCCCCTAGGGGCTGCCCTTGTGTGTGGCGCCACCG GCGGTGGAGAACAAAGGCTCTATTAGCCTGTGCCAGGAAAGGGGATCAGGGGATGCCAG GCATGGACAGTGGGTGGCAGGGGGGAGAGGAGGGCTGTCTGCTTCCCAGAAGTCCAAGGA CACAAATGGGTGAGGGGAGAGCTCTCCCATAGCTGGGCTGCGGCCCAACCCACCCCCTC AGGCTATGCCAGGGGGTGTGCCAGGGGCACCCGGGCATCGCCAGTCTAGCCCACTCCTTC ATAAAGCCCTCGCATCCCAGGAGCGAGCAGAGCCAGAGCAGGTTGGAGAGGAGACGCATCA CCTCCGCTGCTCGCA
4	sgLuc2 <sup>12</sup>	CACCGTTGGCGCTCAACTTTTACGA
5	SgAbca1 (#1)	CACCGGAGAGTCACTCACCCGGACA
6	sgAbca1 (#2)	CACCGTTGGCGCTCAACTTTTACGA
7	sgRNA sequencing primer	TACGTGACGTAGAAAGTA

**Supplementary Table 2. Functional enrichment analysis of tumor-associated astrocytes**

ID	Term ID	Term Name	P <sub>adj</sub>
1	GO:0007049	Cell cycle	2.810x10 <sup>-17</sup>
2	GO:0008152	Metabolic process	7.455x10 <sup>-18</sup>
3	GO:0022402	Cell cycle process	3.882x10 <sup>-19</sup>
4	GO:0034097	Response to cytokine	5.456x10 <sup>-19</sup>
5	GO:0044237	Cellular metabolic process	7.852x10 <sup>-19</sup>
6	GO:0065009	Regulation of molecular function	1.892x10 <sup>-17</sup>
7	GO:0071345	Cellular response to cytokine stimulus	6.642x10 <sup>-18</sup>
8	GO:0071840	Cellular component organization or biogenesis	1.606x10 <sup>-26</sup>
9	GO:1903047	Mitotic cell cycle process	7.675x10 <sup>-17</sup>
10	GO:0000278	Mitotic cell cycle	1.572x10 <sup>-14</sup>
11	GO:0006950	Response to stress	1.257x10 <sup>-15</sup>
12	GO:0010646	Regulation of cell communication	5.250x10 <sup>-16</sup>
13	GO:0071704	Organic substance metabolic process	9.935x10 <sup>-15</sup>
14	GO:0002376	Immune system process	1.398x10 <sup>-11</sup>
15	GO:0006807	Nitrogen compound metabolic process	1.895x10 <sup>-13</sup>
16	GO:0006725	Cellular aromatic compound metabolic process	1.421x10 <sup>-12</sup>
17	GO:0006139	Nucleobase-containing compound metabolic process	2.368x10 <sup>-12</sup>
18	GO:0009893	Positive regulation of metabolic process	9.465x10 <sup>-14</sup>
19	GO:0010604	Positive regulation of macromolecule metabolic process	4.478x10 <sup>-12</sup>
20	GO:0031325	Positive regulation of cellular metabolic process	1.258x10 <sup>-11</sup>
21	GO:0034641	Cellular nitrogen compound metabolic process	1.218x10 <sup>-11</sup>
22	GO:0044238	Primary metabolic process	4.418x10 <sup>-12</sup>
23	GO:0046483	Heterocycle metabolic process	4.138x10 <sup>-13</sup>
24	GO:0051173	Positive regulation of nitrogen compound metabolic process	9.325x10 <sup>-12</sup>
25	GO:0001816	Cytokine production	2.656x10 <sup>-10</sup>
26	GO:0002682	Regulation of immune system process	6.102x10 <sup>-11</sup>
27	GO:0006952	Defense response	1.819x10 <sup>-8</sup>
28	GO:0006260	DNA replication	9.952x10 <sup>-9</sup>
29	GO:0001819	Positive regulation of cytokine production	7.640x10 <sup>-8</sup>
30	GO:0006261	DNA-dependent DNA replication	7.931x10 <sup>-7</sup>
31	GO:0008283	Cell population proliferation	6.102x10 <sup>-8</sup>
32	GO:0010547	Positive regulation of cell communication	4.337x10 <sup>-9</sup>
33	GO:0031347	Regulation of defense response	2.701x10 <sup>-10</sup>
34	GO:0031349	Positive regulation of defense response	2.801x10 <sup>-8</sup>
35	GO:0035458	Cellular response to interferon-beta	1.396x10 <sup>-7</sup>
36	GO:0044260	Cellular macromolecule metabolic process	4.949x10 <sup>-8</sup>
37	GO:0044770	Cell cycle phase transition	2.302x10 <sup>-9</sup>
38	GO:0044085	Cellular component biogenesis	2.027x10 <sup>-10</sup>
39	GO:0043170	Macromolecule metabolic process	2.001x10 <sup>-10</sup>
40	GO:0051301	Cell division	1.971x10 <sup>-9</sup>
41	GO:0051726	Regulation of cell cycle	2.324x10 <sup>-8</sup>
42	GO:0090304	Nucleic acid metabolic process	1.122x10 <sup>-10</sup>
43	GO:1901987	Regulation of cell cycle phase transition	7.436x10 <sup>-8</sup>
44	GO:1901990	Regulation of mitotic cell cycle phase transition	1.709x10 <sup>-7</sup>
45	GO:0045935	Positive regulation of nucleobase-containing compound metabolic process	2.624x10 <sup>-7</sup>
46	GO:0042127	Regulation of cell population proliferation	4.890x10 <sup>-7</sup>
47	GO:0034645	Cellular macromolecule biosynthetic process	3.575x10 <sup>-6</sup>
48	GO:0033993	Response to lipid	7.113x10 <sup>-6</sup>
49	GO:0031323	Regulation of cellular metabolic process	6.053x10 <sup>-6</sup>
50	GO:0019222	Regulation of metabolic process	1.206x10 <sup>-6</sup>
51	GO:0008284	Positive regulation of cell population proliferation	2.054x10 <sup>-5</sup>
52	GO:0002263	Cell activated involved in immune response	5.501x10 <sup>-5</sup>
53	GO:0000280	Nuclear division	1.370x10 <sup>-6</sup>
54	GO:0000082	G1/S transition of mitotic cell cycle	1.451x10 <sup>-4</sup>
55	GO:0002697	Regulation of immune effector process	1.190x10 <sup>-4</sup>
56	GO:0006955	Immune response	9.476x10 <sup>-4</sup>
57	GO:0008608	Attachment of spindle microtubules to kinetochore	3.878x10 <sup>-3</sup>
58	GO:0019221	Cytokine-mediated signaling pathway	2.007x10 <sup>-4</sup>
59	GO:0030335	Positive regulation of cell migration	9.829x10 <sup>-5</sup>
60	GO:0032270	Positive regulation of cellular protein metabolic process	7.465x10 <sup>-5</sup>
61	GO:0050776	Regulation of immune response	1.550x10 <sup>-5</sup>
62	GO:0060255	Regulation of macromolecule metabolic process	1.416x10 <sup>-6</sup>
63	GO:0060759	Regulation of response to cytokine stimulus	6.124x10 <sup>-5</sup>
64	GO:0080090	Regulation of primary metabolic process	2.290x10 <sup>-5</sup>
65	GO:1902806	Regulation of cell cycle G1/S phase transition	3.190x10 <sup>-3</sup>
66	GO:0140014	Mitotic nuclear division	1.703x10 <sup>-5</sup>

67	GO:0060760	Positive regulation of response to cytokine stimulus	$1.187 \times 10^{-3}$
68	GO:0051247	Positive regulation of protein metabolic process	$3.679 \times 10^{-4}$
69	GO:0010556	Regulation of macromolecule biosynthetic process	$3.854 \times 10^{-4}$
70	GO:0006091	Generation of precursor metabolites and energy	$5.548 \times 10^{-4}$

**Supplementary Table 2.** Functional enrichment analysis of differently regulated transcripts from tumor-associated astrocytes based on Gene Ontology (GO).



**Supplementary Table 3. Functional enrichment analysis of human tumor-associated astrocytes**

ID	Term ID	Term Name	ES	FDR
1	R-HSA-3656243	Defective ST3GAL3 causes MCT12 and EIEE15	0.98662	0.03965
2	R-HSA-191273	Cholesterol biosynthesis	0.64482	0.03965
3	R-HSA-389661	Glyoxylate metabolism and glycine degradation	0.63704	0.03965
4	R-HSA-6799198	Complex I biogenesis	0.55068	0.03965
5	R-HSA-163200	Respiratory electron transport, ATP synthesis by chemiosmotic coupling, and heat production by uncoupling proteins.	0.5376	0.03965
6	R-HSA-611105	Respiratory electron transport	0.5357	0.03965
7	R-HSA-1655829	Regulation of cholesterol biosynthesis by SREBP (SREBF)	0.52005	0.03965
8	R-HSA-2426168	Activation of gene expression by SREBF (SREBP)	0.51517	0.03965
9	R-HSA-1428517	The citric acid (TCA) cycle and respiratory electron transport	0.43726	0.03965
10	R-HSA-168249	Innate Immune System	-0.30387	0.03965
11	R-HSA-9006934	Signaling by Receptor Tyrosine Kinases	-0.33193	0.03965
12	R-HSA-372790	Signaling by GPCR	-0.33459	0.03965
13	R-HSA-196854	Metabolism of vitamins and cofactors	-0.38108	0.03965
14	R-HSA-425407	SLC-mediated transmembrane transport	-0.39824	0.03965
15	R-HSA-1280215	Cytokine Signaling in Immune system	-0.39854	0.03965
16	R-HSA-913531	Interferon Signaling	-0.42312	0.03965
17	R-HSA-373760	LICAM interactions	-0.42924	0.03965
18	R-HSA-449147	Signaling by Interleukins	-0.44046	0.03965
19	R-HSA-500792	GPCR ligand binding	-0.45853	0.03965
20	R-HSA-373755	Semaphorin interactions	-0.46668	0.03965
21	R-HSA-6806834	Signaling by MET	-0.51052	0.03965
22	R-HSA-76005	Response to elevated platelet cytosolic Ca2+	-0.53623	0.03965
23	R-HSA-909733	Interferon alpha/beta signaling	-0.53748	0.03965
24	R-HSA-3000178	ECM proteoglycans	-0.58288	0.03965
25	R-HSA-3000171	Non-integrin membrane-ECM interactions	-0.60099	0.03965
26	R-HSA-202733	Cell surface interactions at the vascular wall	-0.60219	0.03965
27	R-HSA-373076	Class A/I (Rhodopsin-like receptors)	-0.61315	0.03965
28	R-HSA-1566948	Elastic fibre formation	-0.62358	0.03965
29	R-HSA-1474244	Extracellular matrix organization	-0.62407	0.03965
30	R-HSA-375276	Peptide ligand-binding receptors	-0.63294	0.03965
31	R-HSA-6785807	Interleukin-4 and Interleukin-13 signaling	-0.63426	0.03965
32	R-HSA-400685	Sema4D in semaphorin signaling	-0.63503	0.03965
33	R-HSA-381426	Regulation of Insulin-like Growth Factor (IGF) transport and uptake by Insulin-like Growth Factor Binding Proteins (IGFBPs)	-0.64225	0.03965
34	R-HSA-9645723	Diseases of programmed cell death	-0.65146	0.03965
35	R-HSA-8875878	MET promotes cell motility	-0.65289	0.03965
36	R-HSA-1442490	Collagen degradation	-0.65325	0.03965
37	R-HSA-6783589	Interleukin-6 family signaling	-0.65494	0.03965
38	R-HSA-877300	Interferon gamma signaling	-0.66473	0.03965
39	R-HSA-76009	Platelet Aggregation (Plug Formation)	-0.6806	0.03965
40	R-HSA-1474228	Degradation of the extracellular matrix	-0.68368	0.03965
41	R-HSA-449836	Other interleukin signaling	-0.68368	0.03965
42	R-HSA-210991	Basigin interactions	-0.68665	0.03965
43	R-HSA-3000170	Syndecan interactions	-0.69992	0.03965
44	R-HSA-3000157	Laminin interactions	-0.71571	0.03965
45	R-HSA-8874081	MET activates PTK2 signaling	-0.7177	0.03965
46	R-HSA-1650814	Collagen biosynthesis and modifying enzymes	-0.71836	0.03965
47	R-HSA-8948216	Collagen chain trimerization	-0.73086	0.03965
48	R-HSA-198933	Immunoregulatory interactions between a Lymphoid and a non-Lymphoid cell	-0.73656	0.03965
49	R-HSA-1474290	Collagen formation	-0.73969	0.03965
50	R-HSA-5357786	TNFR1-induced proapoptotic signaling	-0.74918	0.03965
51	R-HSA-446353	Cell-extracellular matrix interactions	-0.77086	0.03965
52	R-HSA-216083	Integrin cell surface interactions	-0.77262	0.03965
53	R-HSA-196807	Nicotinate metabolism	-0.77888	0.03965
54	R-HSA-2022090	Assembly of collagen fibrils and other multimeric structures	-0.79098	0.03965
55	R-HSA-197264	Nicotinamide salvaging	-0.8154	0.03965
56	R-HSA-6783783	Interleukin-10 signaling	-0.885	0.03965
57	R-HSA-380108	Chemokine receptors bind chemokines	-0.91066	0.03965
58	R-HSA-2243919	Crosslinking of collagen fibrils	-0.93	0.03965
59	R-HSA-173736	Alternative complement activation	-0.9999	0.03965
60	R-HSA-6799990	Metal sequestration by antimicrobial proteins	-1	0.03965

**Supplementary Table 3.** Functional enrichment analysis of differently regulated transcripts from human tumor-associated astrocytes<sup>4</sup> based on the Reactome database. ES - enrichment score comparing the two clusters, FDR - false discovery rate. FDR<0.05.

## Supplementary References

1. Buch T, Heppner FL, Tertilt C, *et al.* A Cre-inducible diphtheria toxin receptor mediates cell lineage ablation after toxin administration. *Nat Methods*. Jun 2005;2(6):419-26.  
doi:10.1038/nmeth762
2. Schreiner B, Romanelli E, Liberski P, *et al.* Astrocyte Depletion Impairs Redox Homeostasis and Triggers Neuronal Loss in the Adult CNS. *Cell Rep*. Sep 1 2015;12(9):1377-84. doi:10.1016/j.celrep.2015.07.051
3. Takenaka MC, Gabriely G, Rothhammer V, *et al.* Control of tumor-associated macrophages and T cells in glioblastoma via AHR and CD39. *Nat Neurosci*. May 2019;22(5):729-740. doi:10.1038/s41593-019-0370-y
4. Darmanis S, Sloan SA, Croote D, *et al.* Single-Cell RNA-Seq Analysis of Infiltrating Neoplastic Cells at the Migrating Front of Human Glioblastoma. *Cell Rep*. Oct 31 2017;21(5):1399-1410. doi:10.1016/j.celrep.2017.10.030
5. Wu YE, Pan L, Zuo Y, Li X, Hong W. Detecting Activated Cell Populations Using Single-Cell RNA-Seq. *Neuron*. Oct 11 2017;96(2):313-329 e6.  
doi:10.1016/j.neuron.2017.09.026
6. Zhong S, Zhang S, Fan X, *et al.* A single-cell RNA-seq survey of the developmental landscape of the human prefrontal cortex. *Nature*. Mar 22 2018;555(7697):524-528.  
doi:10.1038/nature25980
7. Collardeau-Frachon S, Scoazec JY. Vascular development and differentiation during human liver organogenesis. *Anat Rec (Hoboken)*. Jun 2008;291(6):614-27. doi:10.1002/ar.20679

8. Kambach DM, Halim AS, Cauer AG, *et al.* Disabled cell density sensing leads to dysregulated cholesterol synthesis in glioblastoma. *Oncotarget*. Feb 28 2017;8(9):14860-14875. doi:10.18632/oncotarget.14740
9. Lin L, Desai R, Wang X, Lo EH, Xing C. Characteristics of primary rat microglia isolated from mixed cultures using two different methods. *J Neuroinflammation*. May 8 2017;14(1):101. doi:10.1186/s12974-017-0877-7
10. Villa GR, Hulce JJ, Zanca C, *et al.* An LXR-Cholesterol Axis Creates a Metabolic Co-Dependency for Brain Cancers. *Cancer Cell*. Nov 14 2016;30(5):683-693. doi:10.1016/j.ccell.2016.09.008
11. Mayo L, Trauger SA, Blain M, *et al.* Regulation of astrocyte activation by glycolipids drives chronic CNS inflammation. *Nat Med*. Oct 2014;20(10):1147-56. doi:10.1038/nm.3681
12. Hart T, Chandrashekar M, Aregger M, *et al.* High-Resolution CRISPR Screens Reveal Fitness Genes and Genotype-Specific Cancer Liabilities. *Cell*. Dec 3 2015;163(6):1515-26. doi:10.1016/j.cell.2015.11.015